Title

High Throughput Computational Search for Lead-Free Piezoelectric Materials

Author

Ling, Handong

Publication Date

2022

Peer reviewed|Thesis/dissertation

High Throughput Computational Search for Lead-Free Piezoelectric Materials

by

Handong Ling

A dissertation submitted for the degree of

Doctor of Philosophy

in

Engineering - Material Science and Engineering

in the

Graduate Division

of the

University of California, Berkeley

Dissertation Committee:

Professor Kristin A. Persson
Professor Mark Aska
Professor Jeffrey Neaton

Spring 2022

High Throughput Computational Search for Lead-Free Piezoelectric Materials

Table of Contents

Acknowledgements

This work was primarily supported by the Center for Next Generation Materials by Design, an Energy Frontier Research Center funded by the U.S. Department of Energy, Office of Science, Basic Energy Sciences under Award DE-AC02- 05CH11231. Data infrastructure, algorithms and software development was supported by the Materials Project, funded by the U.S. Department of Energy, Office of Science, Office of Basic Energy Sciences, Materials Sciences and Engineering Division under Contract no. DE-AC02-05-CH11231: Materials Project program KC23MP. Computational resources were provided by the National Energy Research Scientific Computing Center, a DOE Office of Science User Facility supported by the Office of Science of the DOE under Contract No. DE-AC02- 05CH11231.

This work was initially supervised by Dr. Shyam Dwarkanath who was crucial to its direction as well as my advisor Professor Kristin Persson. The experimental work was conducted by Megha Acharya under the advisement of Lane Martin, which was crucial to this work. I would also like to thank Kara Fong and Oxana Andriuc for their discussions on science, but mainly topics of non-scholarly fields.

The work in Chapter 2 was supervised by Dr. Shyam Dwarkanath and Professor Kristin Persson. The computational effort in Chapter 3 was supervised by Professor Kristin Persson while the experimental work was led by Megha Archarya and supervised by Professor Lane Martin. The work in Chapter 4 was supervised by Muratahan Aykol, Linda Hung, Joseph Monotoya and Kristin Persson. Co-authored work is reproduced here with permission from all authors.

Abstract

High Throughput Computational Search for Lead-Free Piezoelectric Materials

by

Handong Ling

Doctor of Philosophy in Material Science and Engineering

University of California, Berkeley

Professor Kristin A. Persson, Chair

Ab initio methods provide a powerful tool in the search for novel polar materials. In particular, there have been efforts to identify lead-free piezoelectric material systems to replace $PbZr_{0.52}Ti_{0.48}O_3$. This work first utilizes the Materials Project database of piezoelectric tensors to develop a design rule for disorder-tolerant piezoelectric materials based on the presence of multiple stable optical phonon modes which contribute to the polar response. This criteria is used to produce novel materials with large computationally predicted response. A methodology for exploring alloy systems utilizing a Vegard's law-like linear interpolation of properties is then developed to capitalize on these identified disorder-tolerant materials. A parent ferroelectric $Sr_2Nb_2O_7$ compound is chosen as a parent material for which all reasonable isovalent cation substitutions are considered and explored. Based on our approximations, thermodynamic analysis and density-functional theory (DFT) validation of the large scale system, $Sr_2Nb_{2-2x}V_{2x}O_7$ arises as a promising polar system. $Sr_2Nb_{2-2x}V_{2x}O_7$ is synthesized as single-crystalline thin-film heterostructures using pulsed-laser deposition and an enhanced dielectric response is observed at x = 0.05 and x = 0.1. This alloy and methodology are presented to aid the search for additional lead-free piezoelectric systems to replace $PbZr_{0.52}Ti_{0.48}O_3$ (PZT). Finally we present a software package, Automated X-Ray Diffraction to Structure (AXS), to aid in the materials discovery bottleneck of characterization. The algorithm is based solely on symmetry considerations, and an efficient structure generation algorithm coupled with DFT. AXS is benchmarked against a diverse dataset of structures for which is solves 92% of cases and is also demonstrated to provide ground state structures for showcased experimental systems.

Chapter 1

Introduction

1.1 Computational Search for Lead-Free Piezoelectrics

Piezoelectric materials are ubiquitous devices in modern day electronics as actuators, transducers, sensors, and energy harvestors. However, the most commonly used piezoelectric, $PbZr_{0.52}Ti_{0.48}O_3$ (PZT), is in dire need of replacement due to global regulation of lead as a hazardous element.[1] While the issue of replacing PZT has proven to be quite difficult, piezoelectricity is not a particularly uncommon - any material without inversion symmetry (21 out of the 32 crystallographic point groups) exhibit this property. Piezoelectric materials are those that exhibits a strain when placed in a external electric field. There are four piezoelectric coefficients depending on how we would like to quantify the electric field vs. polarization and stress vs. strain. For the purposes of this computational study, we will consider the piezoelectric coefficient:

$$e_{\alpha j} = \frac{\partial P_\alpha}{\partial \eta_j} \tag{1}$$

where $e_{\alpha j}$ is the piezoelectric coefficient, P_α is the polarization in the α direction, and η_j is the strain of deformation j. PZT is particularly useful for devices due to its anomalously large piezoelectric response and temperature stability. PZT is also chemically inert and relatively inexpensive to manufacture - key components for commercialization. Therefore, PZT has become the dominant chemistry for piezoelectric devices since its discovery in 1952 by the Tokyo Institute and characterization of discontinuous polar properties near the morphotropic phase boundary (MPB) by Jaffe et al in 1954.[2,3] Similar perovskite systems have been researched as candidates to replace PZT including, $K_xNa_{1-x}NbO_3$ (KNN), and $Bi_{0.5}Na_{0.5}TiO_3$ (BNT), which form solid solution disordered alloys near similar MPB. However, these alternatives do not yet exhibit the processing control, temperature stability, and piezoelectric efficiency to entirely replace PZT.[4]

In this work, we utilize the wealth of materials data afforded by the Materials Project alongside *ab initio* methods to search for lead free-piezoelectric systems. Our primary research aim is to develop a computational approach to understand and explore structures which may behave as strong, stable piezoelectric systems. We first develop design rules for materials which may be alloyed in order to develop enhanced piezoelectric response. We then filter our database utilizing these design rules to search for promising new polar systems. After this initial screening, we develop a framework for exploring disorder-tolerant candidate systems for promising alloys with large polar response. We apply this framework to a parent ferroelectric system, $Sr_2Nb_2O_7$ and synthesize the $Sr_2Nb_{2-2x}V_{2x}O_7$ alloy system through pulsed laser deposition based on promising predicted properties. We hope that the results of this methodology and enhanced polar properties of the $Sr_2Nb_{2-2x}V_{2x}O_7$ system will inspire

further use of this framework to explore novel alloy systems for piezoelectric replacements to PZT. Lastly, we present an automated XRD to structure solution (AXS) methodology to characterize XRD samples in high-throughput. As material systems from computational searches continue to be experimentally realized, we offer this software package to further accelerate the materials discovery process.

1.2 Overview of Piezoelectric Calculations through Density Functional Perturbation Theory

Before we dive into an analysis of the piezoelectric database produced by the Materials Project, we will examine how the piezoelecric tensor is computed. The majority of piezoelectric tensors in this work are computed through a linear response framework implementing density functional perturbation theory (DFPT).[5,6] The basic formalism behind DFPT is that wavefunctions, electron densities, and potentials may be expressed as a Taylor-like perturbation series:[5]

$$X^{\lambda} = X^{(0)} + \lambda X^{(1)} + \lambda^2 X^{(2)} + \lambda^3 X^{(3)} + ...\lambda^n X^{(n)} \tag{2}$$

where λ is a small perturbation and the coefficients are given by:

$$X^{(n)} = \frac{1}{n!}\frac{\delta^n X}{\delta \lambda^n}\bigg|_{\lambda=0} \tag{3}$$

In light of this perturbation series, we examine the Sternheimer equation applied to the Kohn-Sham orbitals, which is obtained by expanding the Kohn-Sham equations to the first order.[7] This formulation will allow us to access the first order wave functions, $\psi_n^{(1)}$ which are crucial to the calculation of piezoelectric properties.

$$H_{KS}^{(0)} - \epsilon_{\alpha}^{(0)}|\psi_{\alpha}^{(1)}\rangle = H_{KS}^{(1)} - \epsilon_{\alpha}^{(1)}|\psi_{\alpha}^{(0)}\rangle \tag{4}$$

where $\psi_{\alpha}^{(0)}$ and $\epsilon_{\alpha}^{(0)}$ are the zeroth order Kohn-Sham wavefunctions and energies for the α orbital in an N-electron system. The Kohn-Sham energy, $H_{KS}^{(0)}$ is given by:

$$H_{KS}^{(0)} = T + v_{ext}(\mathbf{r}) + e^2 \int \frac{\rho(\mathbf{r'})}{|\mathbf{r} - \mathbf{r'}|} + \int \frac{\partial v_{xc}}{\partial \rho(\mathbf{r'})}\rho(\mathbf{r'})d\mathbf{r'} \tag{5}$$

where T is the kinetic energy term, v_{ext} is the external potential, v_{xc} is the exchange correlation potential, and ρ is the electron density. Using the orthogonality condition $\langle\psi_{\alpha}^{(0)}|\psi_{\beta}^{(1)}\rangle = 0$ and left multiplying equation (4) by $\langle\psi_n^{(0)}|$, we can obtain an expression for the first order energy from the wave functions:

$$\epsilon_{\alpha}^{(1)} = \langle\psi_{\alpha}^{(0)}|H_{KS}^{(1)}|\psi_{\alpha}^{(0)}\rangle \tag{6}$$

Finally, we left multiply equation 4 by $\langle\psi_{\beta}^{(0)}|$:

$$|\psi_\alpha^{(1)}\rangle = \sum_{\beta\neq\alpha} \frac{\langle\psi_\beta^{(0)}|H_{KS}^{(1)}|\psi_\alpha^{(0)}\rangle}{\epsilon_\alpha^{(0)} - \epsilon_\beta^{(0)}}|\psi_\beta^{(0)}\rangle \tag{7}$$

As indicated by perturbation series in equation 2, this approximation of the first order wave function is obtained by response to the first order Hamiltonian. The dependence of the Kohn-Sham Hamiltonian on the electron density leads to the coupling of first order wave function equations. These equations form a set of self-consistent linear equations which may be solved by utilizing a perturbing potential in DFPT implementations. By expanding the series in equation 2 to include multiple perturbations, we can similarly develop a formulation for the mixed partial derivatives of energy which determine the piezoelectric tensor. We consider an expansion of multiple perturbations, j_1 and j_2, on a quantity X:[8]

$$X^\lambda = X^{(0)} + \sum_{j_1} \lambda_{j_1} X^{(1)} + \sum_{j_1 j_2} \lambda_{j_1,j_2}^2 X^{(2)} + ... \tag{8}$$

Cutting off this expansion at the second order, we see that the mixed partial derivative of a quantity can be approximated through knowledge of first order changes. In DFT, the mixed derivative of the electronic energy can be expressed as:

$$E_{el}^{j_1,j_2} = \frac{1}{2}(\widetilde{E}_{el}^{j_1,j_2} + \widetilde{E}_{el}^{j_2,j_1}) \tag{9}$$

where,

$$\begin{aligned} E_{el}^{j_1,j_2}\{\psi^{(0)};\psi^{j_1},\psi^{j_2}\} = & \\ & \sum_\alpha \big[\langle\psi_\alpha^{j_1}|H^{(0)} - \epsilon_\alpha^{(0)}|\psi_\alpha^{j_2}\rangle + (\langle\psi_\alpha^{j_1}|v_{ext}^{j_2} + v_{xc}^{j_2}|\psi_\alpha^{(0)}\rangle \\ & \langle\psi_\alpha^{(0)}|v_{ext}^{j_1} + v_{xc}^{j_1}|\psi_\alpha^{j_2}\rangle) + \langle\psi_\alpha^{j_1}|v_{ext}^{j_1,j_2}|\psi_\alpha^{j_1}\rangle \\ & + \frac{1}{2}\int\int \frac{\partial^2 H_{XC}}{\partial\rho(\mathbf{r})\partial\rho(\mathbf{r'})}\Big|_{\rho^{(0)}} \rho^{j_1}(\mathbf{r})\rho^{j_2}(\mathbf{r'})d\mathbf{r}d\mathbf{r'} + \frac{1}{2}\frac{\partial^2 E_{H_{XC}}}{\partial\lambda_{j_1}\partial\lambda_{j_2}}\Big|_{\rho^{(0)}} \end{aligned} \tag{10}$$

The derivation can be found in the work of Gonze et al.[9,5] The mixed derivatives relevant to the piezoelectric tensor (frozen-ion piezoelectric tensor, $\bar{e}_{ij}$, Born effective charges, $Z_{m\alpha}$, internal strain tensor, Λ_{mj}, and the force constant matrix, K_{mn}) are accessible through this formalism:[10]

$$\bar{e}_{\alpha j} = -\frac{\partial^2 E}{\partial\varepsilon_\alpha\partial\eta_j}\Big|_{u,\varepsilon} \tag{11}$$

$$Z_{m\alpha} = -\Omega_0\frac{\partial^2 E}{\partial u_m\partial\varepsilon_\alpha}\Big|_{\eta} \tag{12}$$

$$\Lambda_{mj} = -\Omega_0\frac{\partial^2 E}{\partial u_m\partial\eta_j}\Big|_{\varepsilon} \tag{13}$$

$$K_{mn} = \frac{\partial^2 E}{\partial u_m \partial u_n}\Big|_{\varepsilon,\eta} \tag{14}$$

where ε_α is the electric field in the α direction and u_n is the atomic displacement in the n direction. This DFPT formalism is used for the calculation for the majority of piezoelectric tensors in this work through the Vienna Ab Initio Simulation Package (VASP)[11,12] software. In practice, VASP solves the Sternheimer equation to obtain the linear response of the wave functions. Second derivatives are then calculated utilizing the first order wave functions and finite difference displacement of atomic positions.[12] We also note that the ionic portion of the dynamical matrix can be obtained through the Ewald summation:[13,14,8]

$$\begin{aligned} C_{ion,\kappa\alpha,\kappa'\beta} = \\ Z_K Z_{K'} \Bigg[\sum_{G\neq 0} \frac{4\pi}{\Omega_0} \frac{G_{\alpha'} G_{\beta'}}{G^2} e^{\tau_K - \tau_{K'}} \times \exp(-\frac{G^2}{4\Lambda^2}) - \\ \sum_a \Lambda^3 H^{iso}_{\alpha'\ \beta'}(\Lambda d_{a,\kappa\kappa'}) - \frac{3}{4\sqrt{\pi}} \Lambda^3 \delta_{\kappa\kappa'} \Bigg] \end{aligned} \tag{15}$$

where, Z_K is the charge of ion K, τ is the ion displacement, Λ is a parameter chosen for convergence, and:

$$H^{iso}_{\alpha\beta}(x) = \frac{x_\alpha x_\beta}{x^2} \left[\frac{3}{x^3} \mathrm{erfc}(x) + \frac{2}{\sqrt{\pi}} e^{-x^2} \left(\frac{3}{x^2} + 2 \right) \right] - \delta_{\alpha\beta} \left(\frac{\mathrm{erfc}(x)}{x^3} + \frac{2}{\sqrt{\pi}} \frac{e^{-x^2}}{x^2} \right) \tag{16}$$

The workflow for the calculation of these properties through DFPT and the resulting Materials Project database act as a foundation for the following study on design rules for disorder-tolerant piezoelectric materials.

Chapter 2

Origin of Disorder Tolerance in Piezoelectric Materials and Design of Polar Systems

2.1 Introduction

Piezoelectric materials are critical components in a wide variety of applications such as sensors, alarms, monitors, etc resulting in a global piezoelectric device market that comprises an excess of US$20 billion.[1] However, the most commonly used piezoelectric material, $PbZr_{0.52}Ti_{0.48}O_3$ (PZT), warrants replacement due to the recent global regulation of lead as a hazardous element. PZT is a perovskite alloyed on the B-site near a morphotropic phase boundary (MPB), where the proximity to the MPB allows for a substantial change in the polarization direction with relatively small stress. These systems rely on a crystalline structure with soft optical phonon modes, stabilized through disorder or defects. Promising lead-free candidate systems to replace PZT include the similar perovskite MPB systems, $K_xNa_{1-x}NbO_3$ (KNN), and $Bi_{0.5}Na_{0.5}TiO_3$ (BNT), which form solid solution disordered alloys near the relevant phase boundary. However, these alternatives do not yet exhibit the processing control, temperature stability, and piezoelectric efficiency to entirely replace PZT.[4] Improvements in KNN involve doping of the A and B perovskite sites with elements such as Li, Sb, and Ta which have been shown to improve densification and the piezoelectric response.[15,16,17,18] In lead-free alternatives BNT, and $BiFeO_3$, alloying additions of Mn and other transition metal dopants have increased temperature and processing stability at the cost of piezoelectric response.[19,20,21] However, the magnitude of this decline is modest and still allows for their use as effective piezoelectric materials. The receptiveness of these materials to alloying and dopants near the morphotropic phase boundary is partly due to the inherent tolerance of their piezoelectric response to ionic disorder. As disorder is a necessary component of modern piezoelectric systems, understanding its effect

Formula (MP ID)	$\|e_{ij}\|$ **max** (C/m^2)	**Disorder Site**
Pr_3NF_6 (mp-33319)	83.84	Anion
SiO_2 (mp-557873)	63.03	—
$BaNiO_3$ (mp-19241)	17.83	—
Na_2O (mp-776952)	14.23	—
KBi_2F_7 (mp-675634)	14.00	Cation
$NaBiS_2$ (mp-675531)	10.68	Cation
$LiCo_3OF_5$ (mp-764144)	10.05	Anion
$TlNO_2$ (mp-676400)	8.86	Anion
$SrHfO_3$ (mp-13108)	8.73	—
$RbTaO_3$ (mp-755018)	7.97	—
$\mathbf{PbTi_{0.5}Zr_{0.5}O_3}$ (mp-1079416)	6.87	Cation

Table 1: Top 10 calculated piezoelectrics, as ranked by the largest piezoelectric modulus |eij|, from the Materials Project as of 2017 and PZT at the 50% composition for reference.

on the piezoelectric response is crucial to engineering lead-free piezoelectric systems.

Ab initio efforts also utilize disorder as a key parameter in designing piezoelectric materials. For example, investigations into the AlN system by Thorlander et al.[22] have demonstrated the ability of disorder to enhance the piezoelectric response in wurtzite systems through alloying. For a wide variety of materials including perovskite, wurtzite, and zincblende structures, density functional theory has provided insight into the contributions to increased piezoelectric response with changes in composition.[23,24,25,26,27] These approaches have focused on characterizing the Born effective charge and internal strain tensors to describe the change in piezoelectric response with respect to disorder while the phonon contributions are assumed constant. However, the lattice dynamics of the alloy, which are crucial to MPB systems[15], are often not discussed and the relative importance of Born effective charge and internal strain components has not been assessed in detail.

The Materials Project has developed a database of piezoelectric tensors comprising over 3000 compounds to aid in the search for lead-free piezoelectric materials.[28] However, density functional theory approaches to calculating the piezoelectric tensor are limited in exploring disordered alloys as they are confined to finite unit cells with periodic boundary conditions. Indeed, a large number of promising predicted piezoelectric materials currently in the Materials Project are found to be specific orderings of materials naturally found with partially occupied cation or anion decorations as shown in **Table 1**.[1] It is unknown whether the ordered versions of these experimentally observed disordered materials can be synthesized, and if so, whether disorder (which generally includes defective, alloyed, and doped materials) significantly affects the predicted piezoelectric response. In order to guide a broader structure and chemistry search for novel polar systems through computation, it is necessary to understand how disorder alters the piezoelectric response and how to identify systems in which the piezoelectric response is tolerant to disorder.

In this work, we develop a quantitative measure of the piezoelectric response to ionic disorder. We demonstrate its efficacy by examining the effect of perturbations on materials selected from the Material Project's piezoelectric database. Specifically, we apply a statistical sensitivity analysis approach to explain the polar response to mild disorder in a structurally agnostic manner. This analysis can be applied to all piezoelectric tensors calculated in the framework set by Wu et al. which separates the piezoelectric response into an electronic component and ionic component. The ionic portion is then calculated from the Born effective charges (BEC), internal strain tensor (IST), and force constant matrix (FCM). From this analysis, we examine markers for the defect-tolerance of modern alloy systems and apply this knowledge to identify potentially promising piezoelectric compounds which present both i) strong intrinsic response according the *ab initio* calculations and ii) a resilience under defect-level ionic disorder. We present these compounds as potential high piezoelectric response MPB prototype systems to be further explored, for example through alloying as in the PZT system.

[1] these artificially ordered compounds are approximations of disordered ionic systems due to the limitation of *ab initio* simulations which require exactly specified atomic elements and positions.

2.2 Computational Procedures

The piezoelectric tensor is currently available for 3003 materials in the Materials Project, obtained from density functional perturbation theory (DFPT) calculations.[6,29,5,28] The first-principles calculations in this work are conducted with the Vienna Ab Initio Simulation Package (VASP)[11,12] using the PBE Generalized Gradient Approximation (GGA)[30] + U for the exchange-correlation functional. An energy cut-off for the plane waves is set at 1000 eV with a k-point density of approximately 2,000 per reciprocal atom (pra) for the piezoeletric DFPT calculations. The initial structural relaxations were conducted at an energy cut-off of 520 eV.

The piezoelectric tensor is calculated within density functional perturbation theory as:

$$e_{\alpha j} = \bar{e}_{j\alpha} + \Omega_0^{-1} Z_{m\alpha} (K^{-1})_{mn} \Lambda_{nj} \tag{17}$$

where e is the total piezoelectric tensor, $\bar{e}$ is the electronic or clamped ion contribution to the piezoelectric tensor, and the remaining terms represent the relaxed ion contribution. The relaxed ion contribution consists of the unit cell volume, Ω_0, the Born effective charge Z, the force constant matrix K, and the internal strain tensor, Λ.[10] We neglect the contribution of the electronic term, $\bar{e}$, in this study as it generally does not contribute significantly to the total piezoelectric tensor for the materials currently computed (see Appendix A.1 **Figure 1**). We consider the maximum piezoelectric modulus of the full tensor, $|e_{ij}|$, in this work as the metric for piezoelectric response.

Disorder is modeled by introducing stochastically distributed noise independently to each component of the DFPT calculated piezoelectric tensor: the Born effective charge ($\widetilde{BEC}$), internal strain tensor ($\widetilde{IST}$), and force constant matrix ($\widetilde{FCM}$). These perturbations are meant to approximate the local deviations in the dielectric, internal strain, and lattice dynamics of a material as would be introduced by random site disorder. While the dielectric and internal strain tensors can be thought of site property averages across the bulk disordered material, the force constants cannot be treated as trivially. Disorder has been shown to induce broadening and splitting of phonon branches, not accounted for in our model.[31,32] However, studies into high entropy alloys have determined that averaged force constants accurately reproduce phonon spectra at low frequency and long wavelengths.[33] In our model, only gamma point phonons are considered and low-frequency phonon modes contribute most strongly to the piezoelectric response. We do not assume any relationship between the applied perturbations, and thus randomly sample the effects on each component of the piezoelectric tensor over 500 unique perturbations. To ensure that the disorder is physically constrained, the appropriate symmetries of the tensors are preserved after the addition of noise to the DFPT calculated $\widetilde{BEC}$, $\widetilde{IST}$ and $\widetilde{FCM}$. In addition, sum rules for the Born effective charge tensors and force constant matrices are enforced as well as dynamic stability in the force constants. The procedure for generating the tensors, with correct symmetry and sum rules, is detailed in Appendix A.1 and the codebase for this analysis is available online through Pymatgen in the site_symmetries and piezo_sensitivity modules. Analysis of the dynamical matrix is performed with the Phonopy package.[34]

The magnitude of disorder is controlled by scaling the generated noise tensors to the maximum value of the associated DFPT calculated tensors ($\widetilde{BEC}$, $\widetilde{IST}$ and $\widetilde{FCM}$), then multiplying by a scalar, denominated the disorder parameter: σ. Subsequently, the noise tensors are added to their respective DFPT calculated piezoelectric tensors. We choose a maximum disorder parameter of 0.01 to approximate a 1% change in the site properties. We emphasize that σ does not represent a formal order parameter, but is rather constructed to understand the sensitivity of the piezoelectric response to the three individual components of the relaxed ion contribution.

Chemical substitutions were attempted on structures tolerant to disorder to generate new piezoelectric compounds. Substitutions on the structural prototypes are performed based on similar atomic size, common oxidation states, and valence states. At least 4 cation substitutions were performed on each structural prototype and the highest performing compound calculated was included in **Table 2**.

2.3 Results and Discussion

We first apply the disorder sensitivity analysis to piezoelectric systems which are known to retain strong piezoelectric response upon ionic disorder to demonstrate the empirical efficacy of our disorder model. For these disorder-tolerant systems, we choose perovskite $PbTiO_3$, wurtzite AlN, and $K_3Li_2Nb_5O_{15}$ in the tungsten bronze structure. $PbTiO_3$ represents the endpoint composition of PZT, AlN has been shown to exhibit increased piezoelectric response through alloying and several alloys in the tungsten bronze structure are known to be strong piezoelectrics.[22,4,35,36] The same analysis is then applied to a select number of top, predicted polar candidate materials from the Materials Project (see **Table 1**). We then identify the low-lying optical phonon modes that are primarily responsible for the large piezoelectric response to explain the mechanism of disorder-tolerance in these materials (**Figure 4**). Lattice dynamic properties are then used to identify descriptors and design metrics for defect-tolerance in polar structures, such as perovskites, which retain a strong piezoelectric response under cation/anion disorder. The design metric is subsequently applied to search for new, disorder-tolerant piezoelectric systems which may be optimized to further increase their piezoelectric response through alloying.

2.3.1 Origin of Disorder-tolerance in Current Piezoelectric Materials

Figure 1 shows the effect of perturbations scaled by the disorder parameter, σ, on the modulus of the piezoelectric tensor. These perturbations are applied to the DFPT calculated Born effective charges, internal strain tensors, and force constant matrices, independently. A few observations can be made from the results in **Figure 1**: first, the random noise imposed on the each component has an overall low impact, approximately within a percent, on the piezoelectric response. Secondly, the disorder parameter has an almost equal probability of increasing or decreasing the piezoelectric response, as evidenced by the symmetric cone around the original response from the perfectly ordered material. Therefore, we find that disorder on these properties does not significantly or systematically affect the piezoelectric

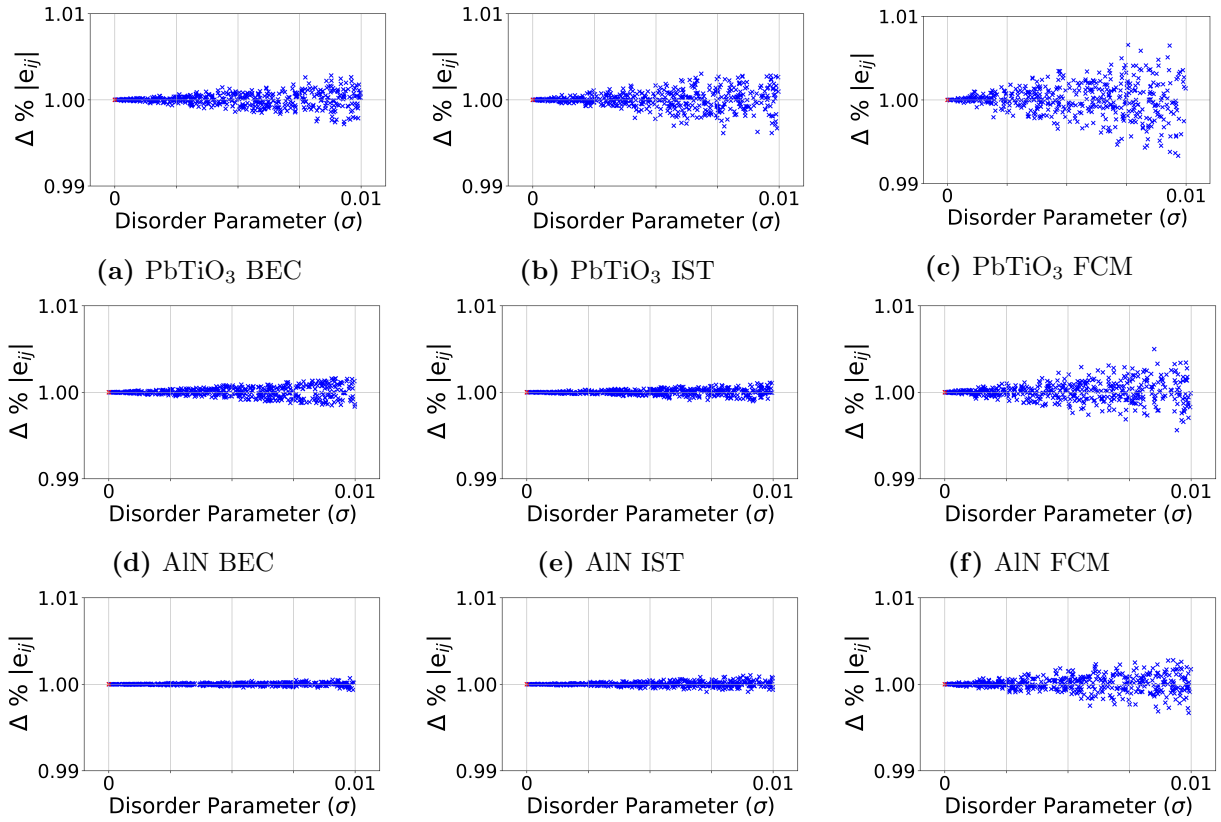

(a) $PbTiO_3$ BEC **(b)** $PbTiO_3$ IST **(c)** $PbTiO_3$ FCM

(d) AlN BEC **(e)** AlN IST **(f)** AlN FCM

(g) $K_3Li_2Nb_5O_{15}$ BEC **(h)** $K_3Li_2Nb_5O_{15}$ IST **(i)** $K_3Li_2Nb_5O_{15}$ FCM

Figure 1: The effect of σ on the maximum modulus of the piezoelectric tensor when applied to the born effective charges (a,d,g), internal strain tensors (b, e, h), and force constant matrices (c, f, i) for $PbTi_{0.5}Zr_{0.5}O_3$, AlN, and $K_3Li_2Nb_5O_{15}$.

response of these materials. This resilience to disorder is consistent with the experimental performance these materials.[37]

Extending to novel systems, we now apply our disorder model to two of the Materials Project's top piezoelectric candidates that exhibit partial occupancies in their as-synthesized form, KBi_2F_7 and Pr_3NF_6, in order to determine their sensitivity to disorder. The results are shown in **Figure 2**. Similar to the known piezoelectrics, when the $\widetilde{BEC}$ and $\widetilde{IST}$ are altered by σ, the piezoelectric modulus shows a nearly random spread around the original response with low amplitude, demonstrating modest effect on the polar response. However, the piezoelectric response of KBi_2F_7 and Pr_3NF_6 show large variation when σ is applied to the $\widetilde{FCM}$. In the case of Pr_3NF_6, disorder tends to show a decline in the piezoelectric response. We therefore note the ability of the force constants, rather than the Born effective charges and internal strain properties, to cause large variation in the piezoelectric response with respect to small perturbations.

To confirm and further examine this apparent sensitivity to disorder, DFPT piezoelectric

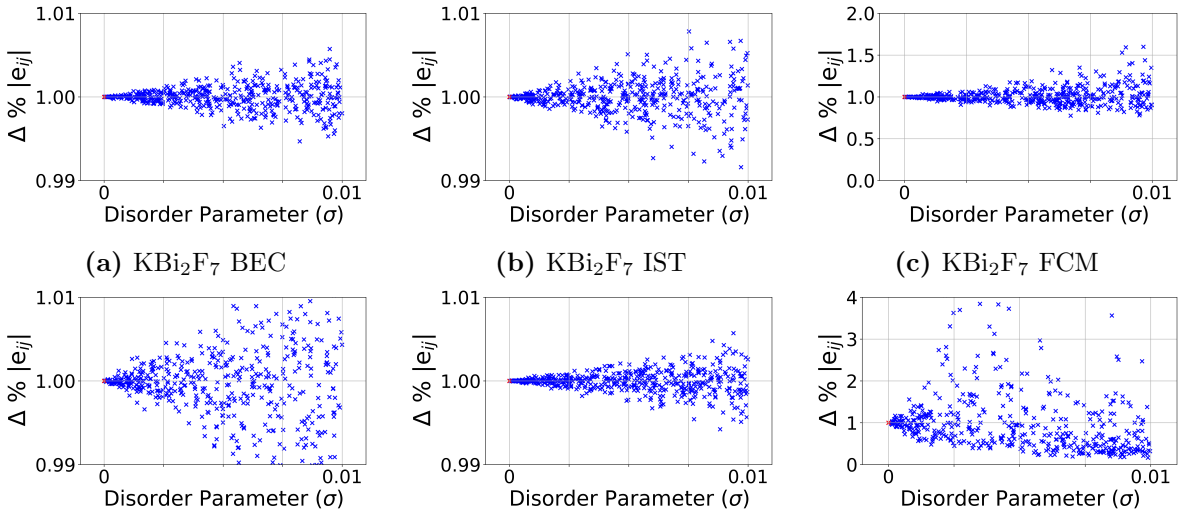

(a) KBi_2F_7 BEC **(b)** KBi_2F_7 IST **(c)** KBi_2F_7 FCM

(d) Pr_3NF_6 BEC **(e)** Pr_3NF_6 IST **(f)** Pr_3NF_6 FCM

Figure 2: The effect of σ on the maximum piezoelectric tensor component when applied to the BEC, IST, and FCM for Pr_3NF_6 and KBi_2F_7.

calculations on varied cation and anion orderings (as found experimentally) of Pr_3NF_6 and KBi_2F_7 were conducted.[38,39] The responses for different orderings are presented in Appendix A.1 **Table 1**. The piezoelectric response is shown to degrade dramatically as the ionic ordering is changed. The sensitivity of the piezoelectric response to the disorder parameter and the degradation of response seen in alternative orderings indicate that these candidate materials would not be suitable for experimental synthesis. On the other hand, changes to the ordering on the B site of PZT at the 50% composition only cause a variation of 3% in the maximum piezoelectric response in DFPT calculations (also shown in Appendix A.1 **Table 1**).

We explore the origin of this sensitivity to disorder by examining the optical phonon modes that contribute to the piezoelectric response by diagonalizing the dynamical matrices

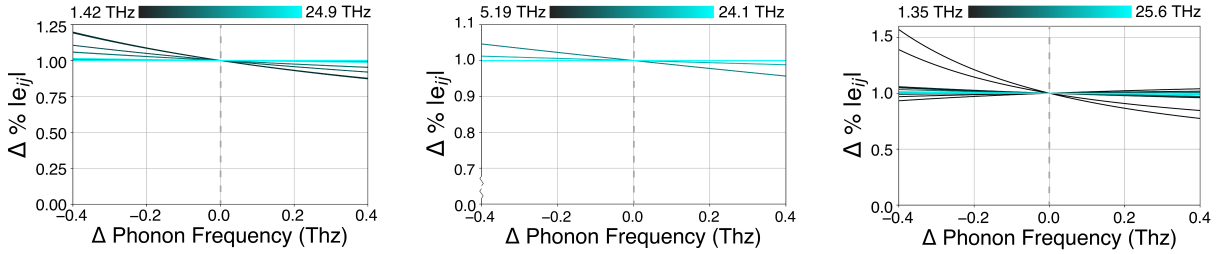

(a) $PbTiO_3$ phonon modes **(b)** AlN phonon modes **(c)** $K_3Li_2Nb_5O_{15}$ phonon modes

Figure 3: The optical phonon frequencies of (a) $PbTiO_3$, (b) AlN, and (c) $K_3Li_2Nb_5O_{15}$ are varied independently to determine the effect of each individual mode on the piezoelectric tensor.

obtained from the DFPT generated force constants. Disorder is known broaden the distribution of phonon frequencies from the ordered lattice phonon spectra which is consistent with the effects of our disorder parameter on the phonon spectra shown in Appendix A.1 **Figure 4**.[33,31] We examine the effects of this broadening on the piezoelectric response by individually altering the phonon frequencies of the disorder-tolerant materials in **Figure 3**.[2] For these perovskite, wurtzite, and tungsten bronze systems, we find that varying the frequency of any individual phonon mode results in a modest decrease in the piezoelectric response, consistent with the trends in **Figure 1**. We also observe a multiplicity of stable optical phonon modes contributing to the piezoelectric response. In these systems, disorder-induced broadening of an individual mode does not significantly alter the piezoelectric response as an individual mode does not dominate the piezoelectric response. In addition, frequency broadening of a single mode may be compensated for by variations in other contributing modes. These structural families exhibit significant piezoelectric response, favorable response to alloying, and large chemical diversity and in these materials, we emphasize the identification of not one, but several stable optical modes in these systems that are associated with a resilience to σ in these materials. Similar trends were found in the DFPT calculated structures of $K_{0.5}Na_{0.5}NbO_3$, and $Bi_{0.5}Na_{0.5}TiO_3$ (SI **Figure 3**). The existence of several modes with significant impact on the polar response is a signature of these highly symmetric perovskite structures and likely a key reason for its dominance among polar materials.

However, in Pr_3NF_6 and KBi_2F_7, which show large variation in the piezoelectric response with σ, we find that a single soft optical mode is responsible for the large response of the perfectly ordered lattice (see **Figure 4**). The frequencies of these phonon modes are the lowest in each material at 0.171 THz in Pr_3NF_6 and 0.433 THz in KBi_2F_7. Conversely, when the frequencies of other optical modes are varied, little to no change in the maximum piezoelectric modulus occurs. DFPT calculations (Appendix A.1 **Table 1**) confirm that this single soft phonon mode is highly sensitive to ionic ordering and controls the degradation of piezoelectric response of these materials. Orderings for other experimentally disordered materials in **Table 1** ($NaBiS_2$ and $TlNO_2$ shown in Appendix A.1 **Table 1**) also support this multiple stable phonon criteria for disorder-tolerance.

In summary, the Born effective charge and internal strain tensor are found to contribute relatively little to the piezoelectric response when perturbed compared to the force constant matrix. We posit that a piezoelectric response that involves several, stable phonon modes is much more likely to exhibit disorder-tolerance, as compared to those involving a singular, soft mode as found in KBi_2F_7 and Pr_3NF_6. We note that both KBi_2F_7 and Pr_3NF_6 are observed experimentally with partial occupancies on their cation/anion lattices, so it is highly unlikely that they exhibit any substantial piezoelectric response in their as-synthesized form as indicated by our sensitivity model and supported by DFPT calculations of varied ionic orderings.

[2] 0.4 THz is chosen from the difference between the softened phonon mode in PZT compared to $PbTiO_3$ which correlates to the largest change in piezoelectric effect (seen in **Figure 4** in the SI).

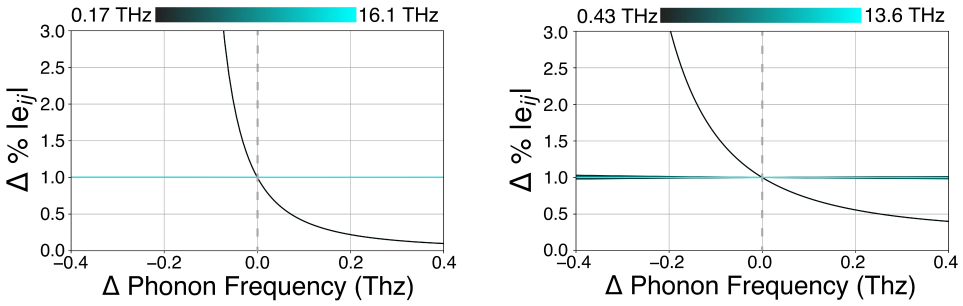

(a) Pr_3NF_6 **(b)** KBi_2F_7

Figure 4: The optical phonon frequencies of (a) Pr_3NF_6 and (b)KBi_2F_7 are varied independently to determine the effect of each individual mode on the piezoelectric tensor.

2.3.2 New Defect-tolerant Piezoelectrics

From the results in the previous section, we observe a strong correlation between a 'disorder-tolerant' piezoelectric response and the existence of *several* optical modes responsible for the favorable piezoelectric distortion. Using this phonon criteria, we present 5 structural prototypes from the Materials Project's 100 highest response piezoelectric materials which show promise as potential MPB systems. These identified prototypes structures are hypothesized to retain large piezoelectric response after alloying. For two of these materials, $ZrZnN_2$ and $Ca_2CoSi_2O_7$, we show the effect of the broadening of phonon frequencies on the piezoelectric response in **Figure 5** to demonstrate the same retention of the polar response as known piezoelectrics under mild disorder (**Figure 3**). These five prototype structures are outside of the perovskite family and include layered configurations (e.g. $NbCl_2O$ and $ZrZnN_2$), rocksalt-like structures (GeTe) and akermanite ($Ca_2CoSi_2O_7$).

For the identified prototype systems, explicit ionic substitutions were explored to deter-

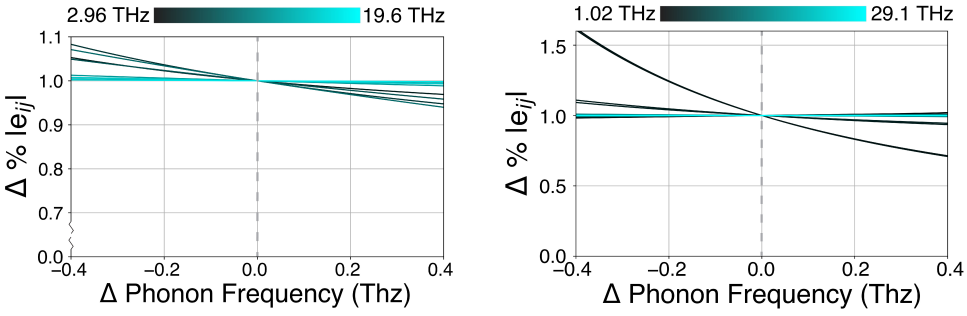

(a) $ZrZnN_2$ phonon modes **(b)** $Ca_2CoSi_2O_7$ phonon modes

Figure 5: The response of the maximum modulus of the piezoelectric tensor with respect to variations in optical phonon frequencies of (a) $ZrZnN_2$ and (b) $Ca_2CoSi_2O_7$ suggest similar behavior to that of the disorder-tolerant, $PbTiO_3$, KNN, and BNT perovksites, as well as AlN and $K_3Li_2Nb_5O_{15}$.

Materials Project Prototype (MP ID)	Prototype $\|e_{ij}\|$ max (C/m^2)	Energy above Hull (eV)	Substitutional Compound (MP ID)	Substitutional Compound $\|e_{ij}\|$ max (C/m^2)	Energy above Hull (eV)	% Change in Piezoelectric Response
$NbCl_2O$ (mp-1025567)	3.78	0.0	VCl_2O (mp-690526)	3.05	0.091	-19.3%
$ZrZnN_2$ (mp-1014244)	2.85	0.0	$ZrHfN_2$ (mp-1224247)	2.51	0.0	-11.8%
GeTe (mp-938)	3.92	0.0	GeSe (N/A)	2.93	0.0	-25.2%
WOF_4 (mp-765135)	2.81	0.0	$MoOF_4$ (N/A)	1.23	0.151	-56.2%
$Ca_2CoSi_2O_7$ (mp-18786)	3.85	0.018	$SrCaCoSi_2O_7$ (N/A)	4.78	0.039	+19.2%

Table 2: The change in piezoelectric response of the identified disorder-tolerant structural prototypes is shown along with the energy above hull before and after the cation replacement. For these structures, large piezoelectric response is still accessible after cation substitution. N/A in the MP ID field identifies a structure not previously calculated in the Materials Project.

mine if the hypothesized disorder-tolerance allows for new chemistries to be discovered from these structural starting points. Several substitutions based on reasonable chemical rules such as ionic size and charge (see Computational Procedures for details) were attempted on the prototype cation sites. The structures were then relaxed and DFPT was utilized to obtain the full piezoelectric tensors. A summary of the results and the chemical substitutions which retain or increase the piezoelectric response of the original compound are shown in **Table 2**. In addition to the maximum piezoelectric response for both prototype compound as well as the substituted material, **Table 2** includes information on the change in piezoelectric response and energy above hull.[3]

The piezoelectric tensors of the substituted materials in **Table 2** were not previously calculated and are all within the top 10% of the Materials Project database in piezoelectric response.[28] This suggests that the cation substituted compounds may be promising candidates for novel piezoelectric materials. However, these materials are also potential endpoints of alloy systems. Each structural prototype will require further investigation with respect to various dopants, orderings, and structural distortions to optimize the piezoelectric response as in the perovskite system. The $SrCaCoSi_2O_7$ system is given as an example of substitution which predicts an increase in the piezoelectric response, highlighting the opportunity to further explore these disorder-tolerant systems through alloying. The nearly 20% increase in piezoelectric response is attributed to softening of specific optical phonons associated with the Sr atoms moving out of phase and pairs of Si tetrahedra flexing or rotating to accommodate this motion. We hypothesize that the $Sr_{2x}Ca_{2-2x}CoSi_2O_7$ system, and many other of these disorder-tolerant systems, may be further investigated to explore the existence of a MPB and hence even greater piezoelectric response.

[3]Energy above hull refers to the energy of decomposition of a material into the most stable compounds at a specific composition. An energy above hull of 0 corresponds to the lowest energy structure at the composition with respect to decomposition to referenced compounds.

2.4 Conclusion

Polar functional materials are dominated by the perovskite structure family, including the leading commercial piezoelectric, PZT. To diversify our portfolio of possible polar functional materials and aid in the design of novel, lead-free piezoelectric materials, the Materials Project recently launched a large search for novel systems, beyond the perovskite family. Interestingly, a larger than expected number of the resulting, predicted high-performing piezoelectrics exhibited a specific ionic ordering while the as-synthezied materials presented partial occupancies. A commercially viable piezoelectric material is likely to employ alloying as a tuning strategy, and hence necessitate retention of its polar response under ionic disorder. To identify such disorder-tolerant polar prototype structures and systems, we develop a statistical sensitivity analysis on the first-principles computed piezoelectric tensor.

Performing the analysis on known, high performing materials ($PbTiO_3$, KNN, BNT, AlN and $K_3Li_2Nb_5O_{15}$) provides insight into the robustness of the perovskite system which exhibits large piezoelectric response under ionic disorder and alloying. While the dielectric and internal strain properties were found to react relatively weakly to the disorder parameter, σ, perturbations to the lattice dynamics are found to heavily control the polar response. Disorder induced broadening of phonon mode frequencies which contribute to the piezoelectric response controls this behavior. Indeed, multiple optical modes in known piezoelectric perovskite systems each contribute significantly to the piezoelectric response, signaling a tolerance to disorder. In contrast, many of the novel computed materials which were predicted to exhibit a large piezoelectric response for a particular ionic ordering, were found to be highly sensitive to even mild ionic disorder. In these materials, a single soft optical phonon mode was responsible for the large polar response. Examples include Pr_3NF_6 and KBi_2F_7 and hence these compounds are excluded as suitable candidates due to the strong disorder-induced degradation in piezoelectric effect. We hope this analysis of lattice dynamics in piezoelectric materials will continue to guide the search for lead-free MPB systems.

The insights gained were used to filter systems in the Materials Project piezoelectric collection for similar disorder-tolerance as the perovskite family. Five structural prototypes were identified. The prototypes were used for explicit cation substitutions and the best performing chemical systems are presented as possible starting points for future alloying strategies. Each of these novel compounds are predicted to exhibit disorder resilience originating from multiple stable optical phonons contributing to the polar response. In addition, the maximum piezoelectric modulus of these materials are within the top 10% of those in the Materials Project. We offer a screening strategy as well as new structural systems to the community in an effort to contribute to the search for novel, environmentally friendly piezoelectrics.

2.5 Application to the Materials Project Database and Associated Limitations

2.5.1 Survey of Promising Candidates and Thermodynamic Stability

The phonon stability criteria described in this work was applied to 100 materials in the Materials Project database with largest piezoelectric responses and dynamically stable phonon modes at the gamma point. The materials which resulted from this screening are identified as amenable to alloying and may be further explored for enhanced piezoelectric response around a potential MPB. However, for many of the materials which passed through initial screening due to their high intrinsic piezoelectric response and lattice dynamic properties, concerns about synthesized bulk properties of the materials led to their removal as candidates. For example, many of these systems were abandoned due to their likelihood of forming centrosymmetric structures in the bulk such as $NaBiS_2$ which is metastable in relation to a rocksalt-like ground state structure in the Materials Project database. In addition, we excluded mixed anion compounds such as $TlNO_2$ and WCl_2O_2, and compounds containing radioactive species or hydrogen which may be difficult to synthesize.

We note that at the time of this work in 2020, the Materials Project contained approxi-

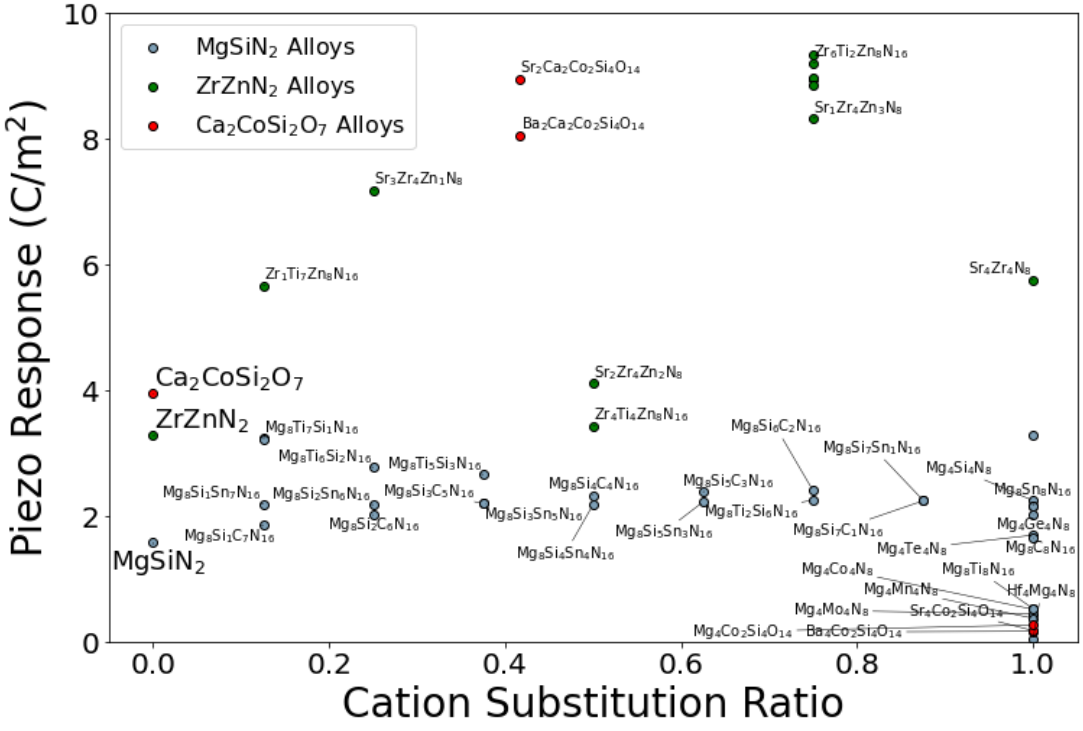

Figure 6: Maximum piezoelectric moduli and for alloys of $ZrZnN_2$, $MgSiN_2$ and $Ca_2CoSi_2O_7$.

mately 1100 piezoelectric tensors with associated force constants for which this analysis could be applied. Currently, the materials project database comprises over 3400 DFPT calculated piezoelectric tensors.

Of the top 100 materials with largest piezoelectric moduli, 47 materials passed our phonon criteria. Of these materials 17 were pervoskite structures. This result is promising due to the known success of disordered alloy systems in the perovskite structural family, but may also be skewed by the representation of perovskite structures in the Materials Project database. While these systems are interesting candidates for further investigation, perovskite systems have been studied in depth and may not provide as many insights as a new structural prototypes. In addition to these perovskites, 10 materials were discarded due to bulk stability and synthesize-ability concerns listed above, leaving 20 candidate material systems. These 20 remaining structures are shown in **Table 3**. Several promising oxide and nitride candidates were identified a result of this analysis: $ZrZnN_2$ and $Ca_2CoSi_2O_7$ as mentioned in the previous study as well as $MgSiN_2$. These materials were chosen for further analysis due to their stability and relatively simple chemistries. Isovalent substitutions on cation sites were explored in order to probe for increased piezoelectric response and are shown in **Figure 6**. We find that

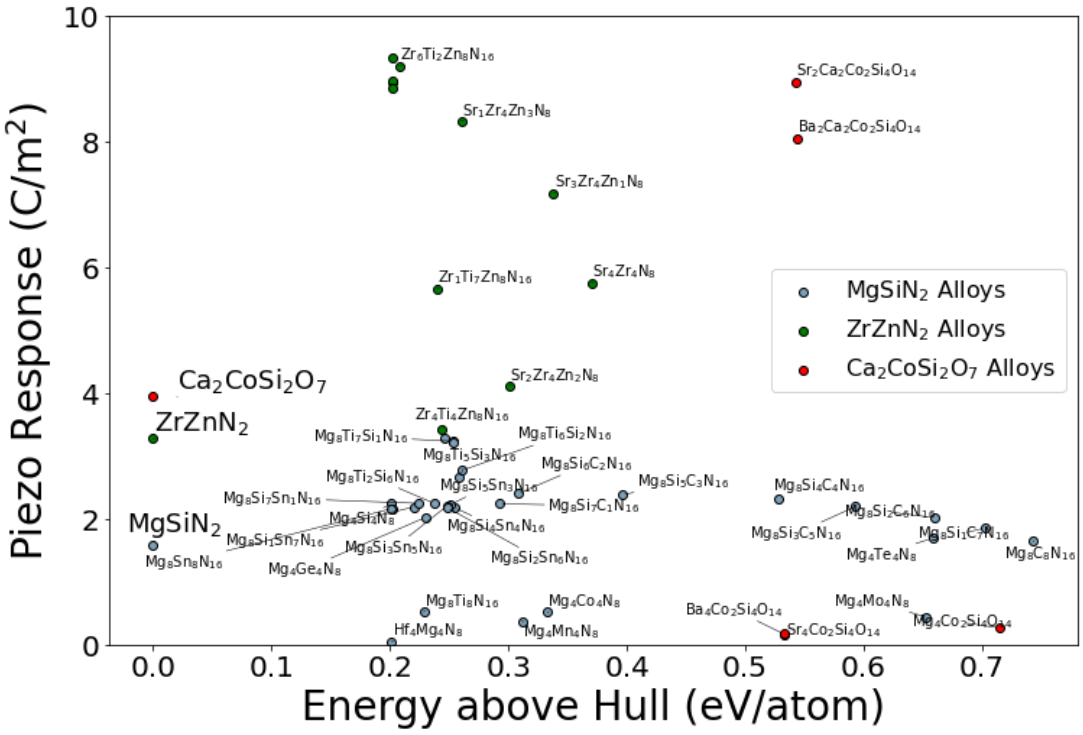

Figure 7: Maximum piezoelectric moduli and energy above hull of various alloys of $ZrZnN_2$, $MgSiN_2$ and $Ca_2CoSi_2O_7$.

for many compositions of $ZrZnN_2$, $MgSiN_2$, and $Ca_2CoSi_2O_7$ alloys, there appear to be alloys with significantly enhanced piezoelectric responses from the endpoint compositions. Some $CaBaCoSi_2O_7$ and $CaSrCoSi_2O_7$ alloys ($SrCaCoSi_2O_7$ and $BaCaCoSi_2O_7$) demonstrate an approximately two-fold increase in piezoelectric response while certain alloys of the $ZrZnN_2$ ($Zr_{0.75}Ti_{0.25}ZnN_2$) system show a three-fold increase. From this brief survey, we find further evidence that the phonon criteria suggested previously can produce predicted material systems with piezoelectric response amenable to alloying. In addition, we find that the intermediate alloying compositions present seemingly fertile grounds for large piezoelectric response, perhaps due to the softening of phonon modes which appear due to partial cation substitutions.

However, these materials can only provide piezoelectric replacements to PZT if they can be synthesized. We use the thermodynamic stability of these alloys as a metric that allows us to estimate the likelihood of successful synthesis. From **Figure 7**, we first find all of the alloy candidates which are more than 0.2 eV/atom above the energy stability hull and therefore unlikely to be metastable.[40] Even if it were possible to stabilize these alloys, it is not clear whether the alloy systems would be able to support solid solutions isostructural to the endpoint compound. Phase segregation or local ordering may significantly affect the polar properties of the material and, therefore, additional calculations must be conducted on multiple orderings of alloy compositions to determine if the solid solution is stable. In addition to these thermodynamic concerns, we must consider that many of these DFT calculated alloy structures contain alternative cation orderings which may produce changes to the piezoelectric response. While not necessarily deleterious, these alternative orderings may provide significantly different piezoelectric responses to those in **Figure 6** at the same composition.

Formula (MP ID)	**$\lvert e_{ij} \rvert$ max (C/m^2)**	**Energy above Hull (eV/atom)**
$ErBiPt$ (mp-30454)	47.54	0
Li_2NiSnO_4 (mp-773418)	16.54	0.013
$SmCu_4Ag$ (mp-867863)	7.61	0.000
Li_2GePbS_4 (mp-19896)	4.46	0.000
$GeTe$ (mp-938)	4.22	0.000
$Ca_2CoSi_2O_7$ (mp-18786)	3.95	0.000
$BiPbF_5$ (mp-35795)	3.87	0.054
$ZrZnN_2$ (mp-1014244)	3.44	0.000
Ag_2S (mp-560025)	3.07	0.085
$VFeSb$ (mp-567636)	2.91	0.000
$TmInPt$ (mp-20103)	2.87	0.000
Zr_3GeO_8 (mp-27888)	2.633	0.003
Li_4MoO_5 (mp-675020)	2.55	0.026
$AlAgS_2$ (mp-7885)	2.39	0.070
$SiPd_2$ (mp-697068)	2.32	0.000
$YbSnRh$ (mp-11973)	2.26	0.000
$TaAsO_4$ (mp-754840)	2.24	0.059
$NbCrO_4$ (mp-754908)	2.23	0.041
Li_2VCrO_4 (mp-755278)	2.16	0.036
$MgSiN_2$ (mp-3677)	1.73	0.000

Table 3: 20 "disorder-tolerant" candidates screened from the Materials Project database for investigation as alloy systems with enhanced piezoelectric response.

$ZrZnN_2$ is a particularly interesting case study on the difficulties of using DFT to model complex solid solution alloys. While the wurtize-like $ZrZnN_2$ structure in the Materials Project database is found to be stable with respect to decomposition to other structures in the database, attempts to experimentally synthesize this structure have produced disordered rocksalt structures common to the nitride space.[41] Large scale DFT calculations of rock salt structures in the $ZrZnN_2$ chemical system confirm the stabilizing effect of disorder against the wurtzite-like structure. Therefore, care must be taken to understand the stabilizing effects of disorder when conducting DFT studies of limited unit cell size.

Although this survey of piezoelectric alloys does in fact find alloys with enhanced piezoelectric response, it is clear that computational studies must consider synthesizeable, as well as large, piezoelectric response material systems. There also exists an added level of difficulty when considering how to explore these alloys in a tractable manner. **Figure 6** and **Figure 7** illustrate the combinitorial issues facing the computational design of a successful piezoelectric alloy systems in DFT. Piezoelectric tensors must be calculated for each cation substitution, composition, and ordering of interest, all while keeping in mind thermodynamic considerations. These piezoelectric and thermodynamic analyses prove even more challenging when considering the computational expense of conducting DFT calculations on unit cells large enough for accurate modeling of solid solution alloys. Therefore, in the following study, we endeavor to develop a framework to thoroughly explore alloy systems for enhanced piezoelectric response and thermodynamic stability in a tractable manner.

Chapter 3

Theory-Guided Exploration of the $Sr_2Nb_2O_7$ System for Increased Dielectric and Piezoelectric Properties and synthesis of Vanadium alloyed $Sr_2Nb_2O_7$

3.1 Introduction

Near morphotrophic phase boundary (MPB) compositions, ceramics may exhibit anomalously large piezoelectric and dielectric properties arising from the flattening of the energy landscape between polarization states.[42] This materials design paradigm has delivered high-performance, technologically successful materials such as $PbZr_{0.52}Ti_{0.48}O_3$ (PZT), which displays both strong piezoelectric as well as dielectric behavior. However, in light of the increasing global restrictions on lead[1], there is strong driving force to identify lead-free piezoelectric replacements. The current, ubiquitous use of PZT in devices is estimated to contribute up to 25% of the total lead in our future electronic waste streams.[1] In addition to environmental concerns, PZT exhibits a Curie temperature of approximately 400° C limiting its use in high-temperature devices.[43]

The majority of current lead-free MPB research is focused on perovskite-structured materials, namely $K_xNa_{1-x}NbO_3$ (KNN), $BiFeO_3$ (BFO), and $Bi_{0.5}Na_{0.5}TiO_3$ (BNT) alloys.[4] These systems all exhibit enhanced polarizability associated with a rhombohedral-to-tetragonal phase transition induced by changes in chemical composition. As a result, their piezoelectric and dielectric properties present solutions for specific applications such as energy harvesters, high-frequency transducers, actuators, and capacitors. However, issues with processing and temperature stability limit these alternative perovskites from providing a generic replacement for PZT.[37] Computational explorations of the perovskite chemical space suggest that more innovation to traditional perovskite structure family may be necessary to provide a successful lead-free competitor to PZT.[44,45] In addition, other structural families, e.g. tungsten bronze, have garnered attention as high temperature solutions.[46]

In this context, computation can serve as a valuable additional resource in the search for possible prototype structures, particularly outside of the traditional rhombohedral-to-tetragonal phase transition perovskites. The Materials Project has developed and benchmarked workflows for the calculation of the full piezoelectric as well as the dielectric tensor.[28,47] To date, these workflows have produced piezoelectric and dielectric tensors for over 3400 and 7100 crystalline materials, respectively. However, these high-throughput density functional theory (DFT) calculations are restricted to bulk, ordered crystals of limited unit-cell size. Strong piezoelectrics, meanwhile, are typically dominated by solid solution disordered alloys, such as PZT, KNN, La or Sm doped BFO, and BNT close to MPBs. In these

alloy systems, the free energy landscape flattens near the solid solution phase boundary, allowing for easy switching of the polarization direction and in turn increased piezoelectric and dielectric response.[42] Therefore, a successful computational search for piezoelectric materials will require the modeling of solid solution alloys near MPBs. However, *ab initio* screening methods have historically focused on ordered materials as the effects of off-stoichiometry and random ionic disorder can be difficult to capture within a limited-size, periodic supercell.

MPBs are characterized by the softening of phonon modes which indicate the emerging preference of the structure to adopt a new structural symmetry.[48,49] Therefore, calculating the lattice dynamic properties as an alloy changes in composition is essential to determining the presence of potential MPBs and enhanced piezoelectric response near the phase boundary. Lattice dynamic properties of solid solutions have been previously modeled by averaging the properties of special quasirandom structures (SQS), generating transferable force constants, or self-consistent phonon approaches.[50,51,52,53,54] Transferable force constants have been used to determine vibrational entropies of mixing for aluminum - transition metal alloys.[51] More recently, self-consistent calculations of phonon modes have been used to generate force constants suitable for molecular dynamics in MoS_2 monolayers.[53] These methods, however, can be computationally expensive for high-throughput searches, limiting the possibility of exploring large solid solution alloy systems.

In this work, we develop a computational methodology to extensively explore candidate piezoelectric alloy systems for increased polar response by using a Vegard's law-like linear approximation to model the Born effective charges, internal stain tensor components, and force constants of an alloy from its compositional endpoints. We first demonstrate the efficacy of this approach on PZT to model the softening phonon modes around the MPB and enhanced polar response associated with the phase transition. We then choose a layered perovskite structure, $Sr_2Nb_2O_7$, and explore the possibility of increased polar response as a function of alloying with a high-throughput framework. Recent work,[55] which focused on identifying defect-tolerant materials and structural classes which retain much of their piezoelectric response with respect to disorder, identified $Sr_2Nb_2O_7$ as a promising parent compound. Layered perovskite $Sr_2Nb_2O_7$ has been synthesized previously and is a known ferroelectric material with a Curie temperature above 1200° C.[56,57] In addition, substitutional alloys systems of $Sr_2Nb_2O_7$ with barium, vanadium and tantalum have also been synthesized demonstrating the ability of this system to support stable, disordered solid solutions.[58,59,60] Focusing on the lattice dynamic properties of this system, we explore suitable substitutions on both the Sr and Nb cation sites for improved piezoeletric and dielectric response near regions of softened phonon modes. We use the Vegard's law-like linear approximation to model the alloy space between the compositional endpoints which allows us to tractably explore alloys systems of the parent $Sr_2Nb_2O_7$ material. Promising alloys are assessed for thermodynamic stability and large scale DFT calculations are employed on the best performing alloy system, $Sr_2Nb_{2-2x}V_{2x}O_7$, in order to validate the linear interpolation approach. Following the recommendations obtained by DFT calculations for enhanced polar behavior, the system is synthesized through pulsed-laser deposition and increased dielectric properties are found. Along with this general methodology for systematically exploring disorder-tolerant[55] piezo-

electric alloy systems, we identify $Sr_2Nb_{2-2x}V_{2x}O_7$ as a promising system with confirmed increased dielectric and predicted increased piezoelectric response.

3.2. Procedures

3.2.1 Computational Procedure

The candidate substitutional alloy systems we consider in the study are $Sr_{2-2x}A_{2x}Nb_2O_7$ and $Sr_2Nb_{2-2x}B_{2x}O_7$, where $A = \{$Ca, Ba$\}$ and $B = \{$As, Au, Bi, Cr, Ir, Mo, N, Os, P, Pt, Re, Rh, Ru, Sb, Ta, V, W$\}$. This includes all non-radioactive elements which were deemed as possible isovalent substitutions on the cation sites i.e. exhibit the same oxidation state and occupy the same coordination environment as in the layered perovskite structured $Sr_2Nb_2O_7$. The Born effective charges, internal strain tensors, and force constants of structures at the endpoints of these alloy systems are calculated using Density Functional Perturbation Theory (DFPT)[6,29,5,28], utilizing the Vienna Ab Initio Simulation Package (VASP)[11,12] within the PBE Generalized Gradient Approximation (GGA+U).[30] An initial structural relaxation is conducted at an energy cut-off of 700 eV. Then an energy cut-off for the plane waves is set at 1000 eV with a k-point density of approximately 2,000 per reciprocal atom (pra) for the piezoeletric DFPT calculations.[10] The Born effective charges and internal strain tensors are atomic site properties calculated for all atoms in the 22-atom orthorhombic unit cell while the force constants are calculated for each atom pair in the unit cell. Subsequently, the piezoelectric tensor in this study is calculated as:

$$e_{\alpha j} = \bar{e}_{j\alpha} + \Omega_0^{-1} Z_{m\alpha} (K^{-1})_{mn} \Lambda_{nj} \tag{18}$$

where e is the total piezoelectric tensor, $\bar{e}$ is the electronic or clamped ion contribution to the piezoelectric tensor, and the remaining terms represent the relaxed ion contribution. The relaxed ion contribution consists of the unit cell volume, Ω_0, the Born effective charge Z, the force constant matrix K, and the internal strain tensor, Λ.[10] Similarly, the dielectric tensor is calculated as:

$$\chi_{\alpha\beta} = \bar{\chi}_{m\alpha} + \Omega_0^{-1} Z_{m\alpha} (K^{-1})_{mn} Z_{n\beta} \tag{19}$$

We note that the dielectric and piezoelectric tensors are often correlated due to the inclusion of the Born effective charges and force constants.[10,43] We neglect the contribution of the electronic term in the piezoelectric calculation, $\bar{e}$, in this study as it generally does not contribute significantly to the total piezoelectric tensor for the materials currently computed in the Materials Project database.[55] Once the piezoelectric properties for the fully substituted alloys are computed, we approximate the piezoelectric tensor for the intermediate compositions of the substitutional alloy systems by employing a Vegard's law-like linear approximation for the Born effective charges, internal stain tensors, and force constants of the alloy. The force constants and associated phonon spectra of alloy systems can be particularly expensive to obtain computationally. Korman *et al.* demonstrated, however, that for long wavelengths and low frequencies relevant to the piezoelectric response, the phonon spectra of high entropy alloys may be reasonably reproduced by averaging force constants

from endpoint compositions.[33] The resulting piezoelectric responses reported in this study are the maximum of the singular values of the total piezoelectric tensor.

The candidate $Sr_{2-2x}A_{2x}Nb_2O_7$ and $Sr_2Nb_{2-2x}B_{2x}O_7$ alloys need to exhibit a stable solid solution such that force constants, Born effective charges, and internal strain properties vary gradually with composition and to allow for the possibility of a MPB to form. Hence, alloy systems are further evaluated for thermodynamic metastability. All possible cation site orderings within a 44-atom unit cell across the selected composition space are enumerated and energies of the relaxed structures are calculated using DFT with an energy cutoff of 700 eV and 1000 k-points per reciprocal atom. Metastability for each ordering in these systems is approximated as 0.1 eV per atom above the hull which captures approximately 80% of experimentally observed metastable oxides.[40] In addition to metastability, a stable solid solution criteria is set at an energy range of 0.025 eV per atom (approximately equal to k_BT at room temperature) between the lowest and highest energy orderings at a given composition.[40]

Finally, for the most promising candidate system $Sr_2Nb_{2-2x}V_{2x}O_7$ which demonstrates a large predicted increase of its piezoelectric and dielectric response, we perform 88-atom supercell calculations to more accurately model the polar response of the disordered system. The calculations of the $Sr_2Nb_{2-2x}V_{2x}O_7$ supercell structure use an energy cut-off of 700 eV and an electronic energy convergence of 10^{-6} eV. Structures are relaxed to a force of less than 0.1 eV/Å and then the Born effective charges, internal strain tensor, and force constant matrices are calculated. The Born effective charges are obtained through DFPT. The internal strain tensor is fitted to forces from 20 strains between -0.01 to 0.01 for each of the cartesian and shear strains. Analyses of the force constants and dynamical matrix are performed with DFT and the Phonopy package.[34] The Born effective charges, internal strain tensors, and force constants are calculated for multiple special quasirandom structures (SQS), obtained through Alloy Threoteic Automated Toolkit (ATAT), to ensure the response was not dependent on a specific cation ordering.[61] These SQSs are chosen such that the generated unit cells contain cluster vectors which most closely match those of truly random alloys so as to construct solid solutions in a mathematically rigorous manner.[61] To compute the dielectric tensors, the electronic portion is calculated through DFPT. The ionic portion of the tensors are calculated from the Born effective charges and force constants as specified in Wu et al.[10]

Piezoelectric tensors and force constants are also calculated for $PbZr_xTi_{1-x}O_3$ compositions (x = 0, 0.25, 0.5, 0.75, 1) through DFPT, with the same parameters as for the layered perovskite systems. For each composition, five 20-atom SQSs are obtained through the ATAT package. The Born effective charges, internal strain tensors and force constants of each SQS at a given composition are then averaged to more accurately capture the properties of the solid solution.[50,61] This procedure is aimed at comparing the force constants generated from a a linear interpolation of endpoint site properties against those generated from multiple SQSs at specific compositions for a well studied system. In this study, the piezoelectric properties of multiple SQSs are averaged by taking the mean of the Born effective charges, internal strain tensors, and force constants for each atomic site between all orderings and then calculating subsequent the piezoelectric tensor for these average properties. Symmetries

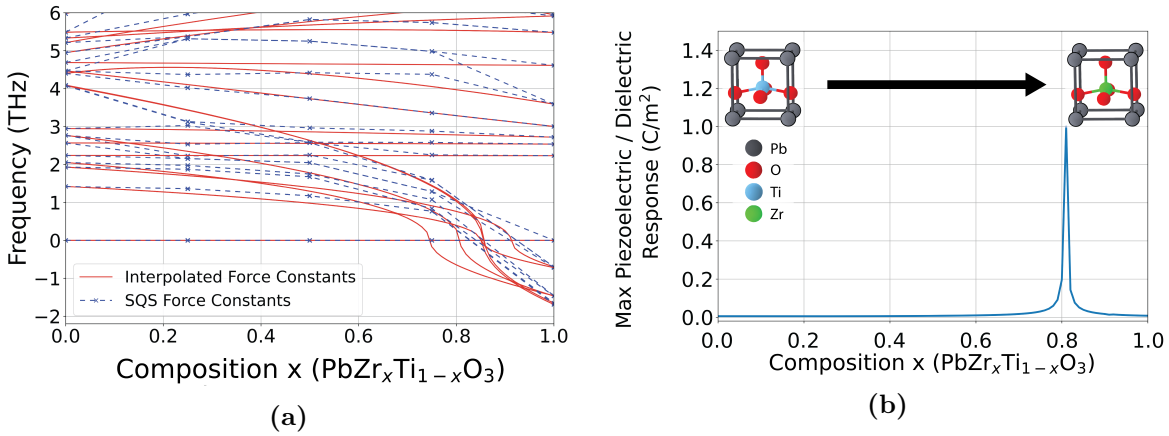

Figure 8: (a.) The gamma point phonon frequencies of the PZT system are plotted from a linear interpolation of force constants in red compared against those calculated from averages of SQS's at varying compositions in blue. (b.) The associated normalized piezoelectric response calculated from the linearly interpolated force constants, Born effective charges, and internal strain tensors of the endpoint compositions generated through DFT

are taken into account by counting each symmetry equivalent transformation of each SQS as a distinct ordering in the mean.

3.2.2 Experimental Procedures

Growth of Thin-Film Heterostructures: The thin-film heterostructures with compositions $Sr_2Nb_{2-2x}V_{2x}O_7$ (x = 0, 0.05, 0.1) were deposited using pulsed-laser deposition in an on-axis geometry with a KrF excimer laser (248 nm, LPX 300, Coherent) and a target-to-substrate distance of 55 mm. Films with a range of thicknesses (50-300 nm) were grown on $SrTiO_3$ (110) substrates over a range of growth conditions using ceramic targets with compositions $Sr_2Nb_2O_7$ and $Sr_2V_2O_7$. The solid solution compositions (i.e., $Sr_2Nb_{2-2x}V_{2x}O_7$, x = 0.05 and 0.1) were first synthesized utilizing alternate ablation from the two parent targets (i.e., $Sr_2Nb_2O_7$ and $Sr_2V_2O_7$) via sub-unit-cell-level mixing using a programmable target rotator (Neocera, LLC) synced with the excimer laser. Next, individual targets with compositions $Sr_2Nb_{2-2x}V_{2x}O_7$ (x = 0.05 and 0.1) were used for synthesizing the final heterostructures. The best results were obtained for the growths performed at a heater temperature of 750°C (for x = 0) and 600°C (for x = 0.05 and 0.1) with a laser fluence of 3.75 J/cm^2 and laser repetition rate of 10 Hz at a dynamic oxygen partial pressure of 100 mTorr. In all cases, 30-45 nm thick $La_{0.7}Sr_{0.3}MnO_3$ films were used as the conductive oxide for the bottom and the top electrodes in the heterostructures. The $La_{0.7}Sr_{0.3}MnO_3$ films were grown at a heater temperature of 750°C with a laser fluence of 2 J/cm^2 at a laser repetition frequency of 2 Hz and a dynamic oxygen partial pressure of 100 mTorr. All the heterostructures were cooled to room temperature from the temperature of growth at a rate of 10°C/min in a static oxygen pressure of 700 Torr.

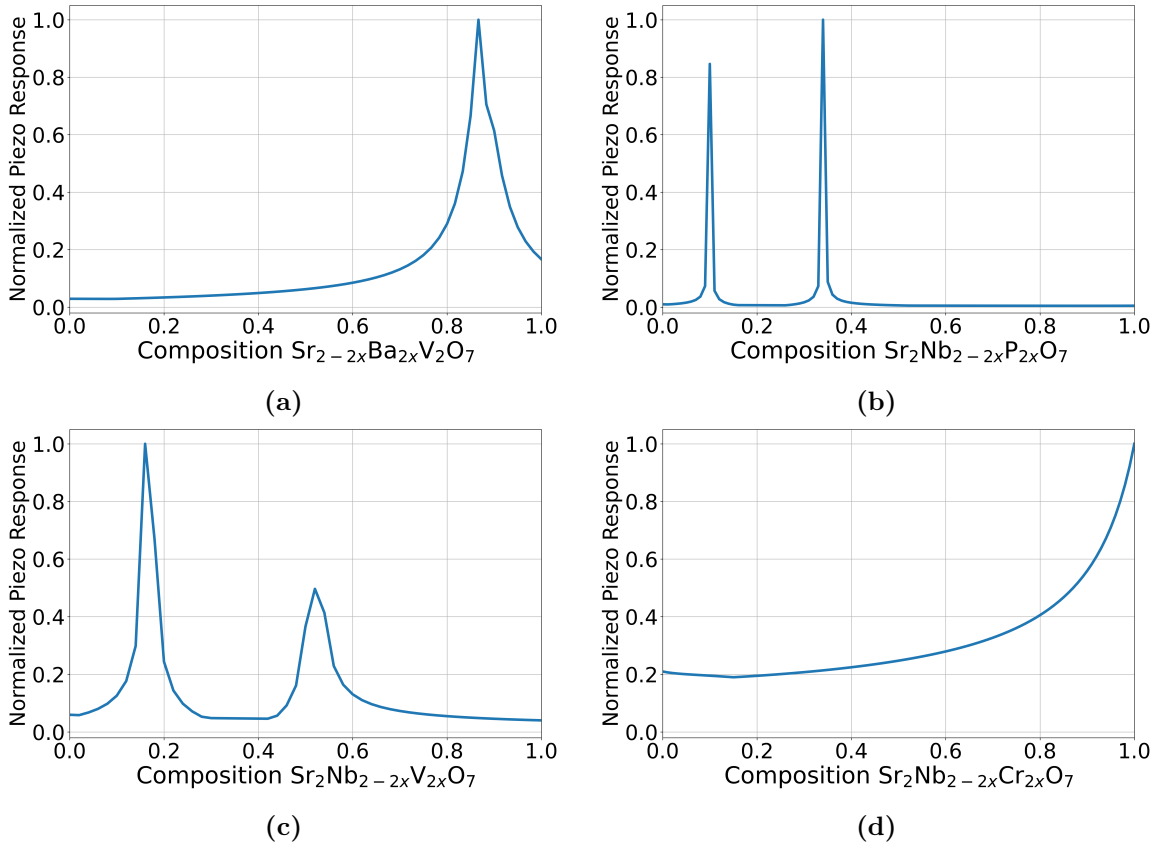

Figure 9: The piezoelectric and dielectric response for alloy systems of the $Sr_2Nb_2O_7$ system as approximated from a linear interpolation of properties from $Sr_{2-2x}A_{2x}Nb_2O_7$ and $Sr_2Nb_{2-2x}B_{2x}O_7$ alloy endpoints. The four alloys shown all contain peaks in the approximated piezoelectric response which indicates the potential for enhancement in response as phonon modes soften during alloying.

Structural Characterization using X-ray diffraction: X-ray diffraction studies were performed using a high-resolution X-ray diffractometer (Panalytical, X'Pert MRD) with a fixed slit of 1/2° in the incident beam optics (copper K_α radiation with $\lambda = 1.54$ Å) and a receiving slit of 0.275 mm in the diffracted beam optics (PIXcel3D-Medipix3 detector). The crystal structure of the synthesized thin-film heterostructures were determined in the direction perpendicular to the plane of the substrate using $\theta - 2\theta$ line scans.

Dielectric Characterization: The dielectric properties for the heterostructures with compositions $Sr_2Nb_{2-2x}V_{2x}O_7$ (x = 0, 0.05, 0.1) were measured using an E4990A Impedance Analyzer (Keysight Technologies) as a function of applied DC electric field strength (-1000 to 1000 kV/cm) at a frequency of 10 kHz.

3.3 Results and Discussion

3.3.1 Linear Approximation to Predict Phonon Softening in $PbZr_xTi_{1-x}O_3$

The primary work of our methodology is to accurately determine properties of intermediate alloy compositions through interpolation from the properties of their endpoint compounds. Therefore, we first demonstrate that linearly interpolating force constants, Born effective charges, and internal strain tensors between the endpoints in the well-studied tetragonal *P4mm* PZT phase yield reasonable predictions of trends in the piezoelectric response with respect to changes in composition. In **Figure 8a**, we plot the normalized piezoelectric and dielectric response associated with these linearly interpolated properties and observe a discontinuous peak in the piezoelectric response at a composition of approximately x = 0.8. We note that the approximated dielectric and piezoelectric response in Figure 8a are identical as both are discontinuous with respect to instabilities in the force constant matrix.

The primary factor contributing to the peak in our approximation of the piezoelectric response is the softening of lattice dynamic properties also observed experimentally in PZT.[49]. In **Figure 8b**, we plot (in red) the gamma point phonon spectra generated from linearly interpolating the DFPT force constants used to produce the piezoelectric response in **Figure 8a**. In order to examine how well linearly interpolated force constants capture lattice dynamic properties at intermediate compositions, we compare to the spectra calculated from averaging multiple SQS force constants. The force constants are calculated for five $PbZr_xTi_{1-x}O_3$ compositions (x = 0, 0.25, 0.5, 0.75, 1). With increasing zirconium content, the phonon modes of the PZT system derived from average SQS results soften and become unstable at approximately x = 0.85. Using the linearly interpolated end-point force constants, we find that the overall trend of phonon modes softening is well described, noting that dynamical instability is predicted at a slightly lower zirconium content (x = 0.75), heralding the experimentally observed structural instability at the MPB. The calculated softening of phonon modes is associated with an increase in polarizability leading to the peak in approximated piezoelectric and dielectric response in **Figure 8a**. Comparing to experimental results, a similar large enhancement of piezoelectric response is observed in PZT, albeit at 52% zirconium.[62] However, it is common for first-order phase transformations to occur before a crystal becomes dynamically unstable and hence the location of maximum piezoelectric response does not necessarily correspond to the composition of approximated dynamical instability of the alloy. We summarize that the experimentally observed presence of a PZT MPB, large increase in the piezoelectric and dielectric response, and softening of the phonon modes associated with the B-site atom distorting the oxygen cage, are all qualitatively well captured by the linearly interpolated force constant methodology.[49] While the softening phonon modes in an alloy do not necessitate the presence of an MPB, they can regardless lead to a predicated enhancement of polar properties. In this PZT system, the approximated phonon instabilities are indeed associated with an MPB which demonstrates the potential for this approximation to act as a high-throughput descriptor for MPBs in alloy systems.

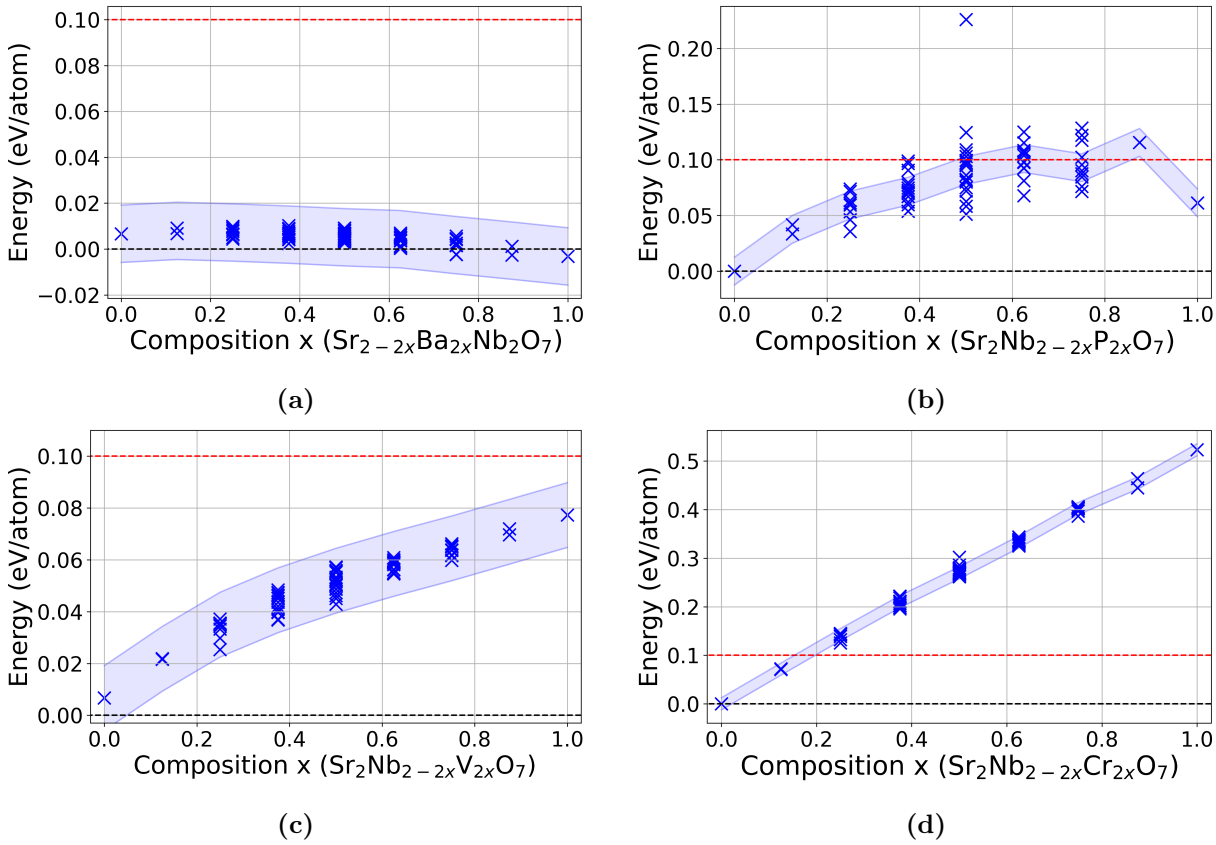

Figure 10: The computed energies above hull of all orderings within 44-atom unit cells of four promising alloy systems are calculated in order to determine guidelines for metastability and solid solution stability. The blue crosses represent structures in the parent $Cmc2_1$ space groups. Criteria for metastable solid solution that structures at a given composition must be below the 0.01 eV/atom above the hull indicated by the red line and within 0.025 eV/atom of each other indicated by the blue shading. The stability hull, as taken from structures in the Materials Project, is shown at an energy of 0 eV/atom as a black line.

3.3.2 Exploration of $Sr_2Nb_2O_7$ Alloy Systems

Subsequently, we utilize linearly interpolated force constants, Born effective charges and internal strain tensors to approximate the piezoelectric response for all candidate alloys originating from the parent $Sr_2Nb_2O_7$ compound. These alloy systems include site substitutions of two elements on the strontium site and 18 elements on the niobium site, as listed in the computational procedures. The approximated piezoelectric response is examined for enhanced response near compositions with softened phonon modes in each of these substitutional systems. We highlight alloy systems with barium substitution on the A site and phosphorous, vanadium, and chromium substitution on the B site as promising potential polar systems based on their approximated response at intermediate compositions shown in **Figure 9**. In these alloy systems, a dramatic increase in the piezoelectric response is asso-

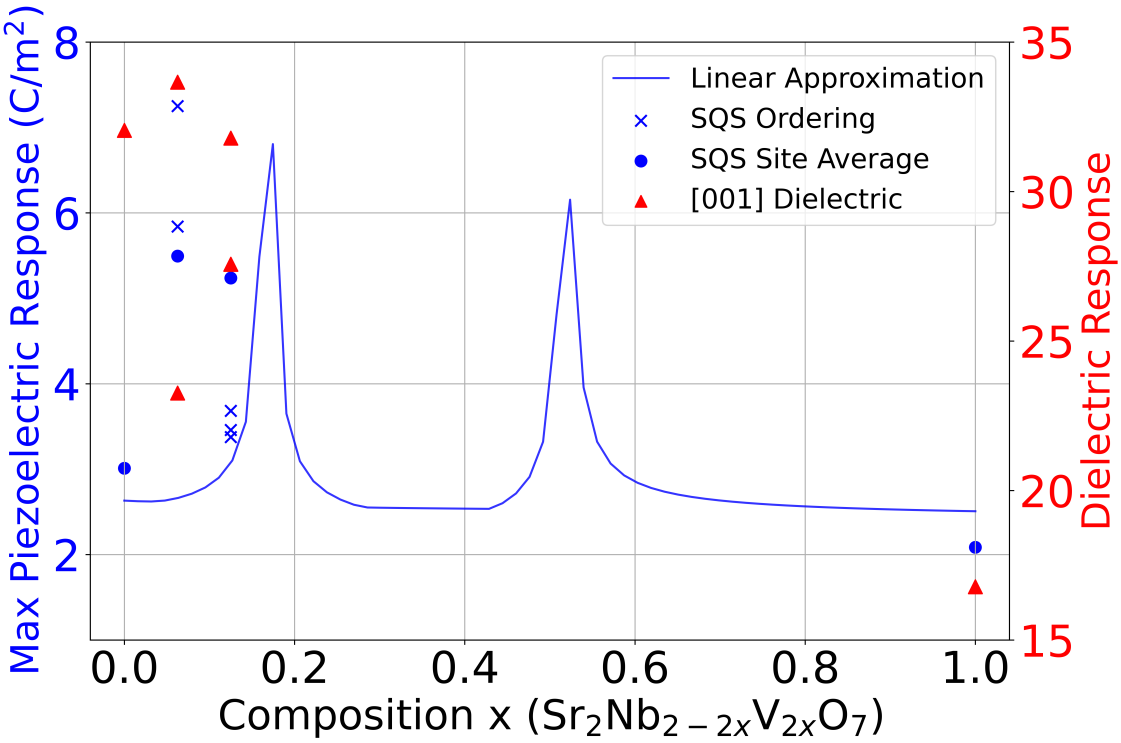

Figure 11: The piezoelectric response of 88-atom unit cells of the $Sr_2Nb_{2-2x}V_{2x}O_7$ system. Three SQS orderings generated from ATAT at x = 0.125 and both unique orderings at x = 0.0625 are shown. The piezoelectric response generated from an average of the force constants, Born effective charges, and internal strain tensors of all orderings at each composition is shown as a solid circle. The approximation generated from a Vegard's law interpolation of properties from $Sr_2Nb_2O_7$ and $Sr_2V_2O_7$ is shown in the background. Dielectric response in the [001] for individual SQS orderings of the structure are shown in red.

ciated with phonon modes softening as a function of alloy composition. All other systems, including those which also demonstrate a discontinuous increase in piezoelectric response but presented a large number of unstable phonon modes, are shown in Appendix A.2 **Figure 1**.

We next take into consideration the thermodynamic stability of alloys from the parent $Sr_2Nb_2O_7$ system. We plot the energy above hull for all possible cation orderings within a 44-atom unit cell of each alloy as a function of composition in **Figure 10**. As previously noted, an energy above hull lower than 0.1 eV per atom suggests metastable ordering, and a maximum energy range less than 0.025 eV per atom at a given composition implies a metastable solid solution as described in Methods.[40] From **Figure 10d**, we find that many orderings of the $Sr_2Nb_{2-2x}Cr_{2x}O_7$ alloy system present steep increases of thermodynamic instability as a function of chromium content (note the considerably larger vertical axis scale), which likely indicates that any attempted alloy at compositions close to the predicted increase in piezoelectric response (see **Figure 9d**) will decompose during synthesis. Therefore we ex-

clude this system from further investigation. **Figure 10b**, suggests that compositions in the $Sr_2Nb_{2-2x}P_{2x}O_7$ alloy systems are unlikely to form solid solutions, especially in the intermediate alloy range 0.2<x<0.8. The maximum piezoelectric response for the $Sr_2Nb_{2-2x}P_{2x}O_7$ system lies around x = 0.1, suggesting that niobium rich versions of this alloy may present viable candidates to form solid solutions with enhanced response. In particular, from **Figure 10a** and **10c** we note that $Sr_{2-2x}Ba_{2x}Nb_2O_7$ and $Sr_2Nb_{2-2x}V_{2x}O_7$ alloys are metastable throughout the composition range and likely amenable to present as solid solutions. For the purposes of this study, we will consider the $Sr_2Nb_{2-2x}V_{2x}O_7$ system for further study as the barium substituted compound has been synthesized and was shown to form a $Ba_5Nb_4O_{15}$ secondary phase.[49]

Focusing on the $Sr_2Nb_{2-2x}V_{2x}O_7$ system, we further explore the approximation of large piezoelectric response by constructing an 88-atom system and computing the piezoelectric and dielectric response at select compositions.[34] The piezoelectric response generated from linear approximations of endpoint properties (**Figure 9c**), as well as the thermodynamic stability window (**Figure 10c**), indicates that compositions below 20% vanadium composition are likely to produce stable materials in the layered perovskite structure with large piezoelectric response. For these reasons, we choose compositions of x = 0.0625 and 0.125 to conduct these large scale DFT calculations.

Figure 11 shows the results of DFT calculations of the polar properties for 88-atom unit cell $Sr_2Nb_{2-2x}V_{2x}O_7$ alloys. In order to demonstrate the effect of specific orderings on the piezoelectric and dielectric response, we calculate the tensors for both unique sites at the x = 0.0625 composition and three distinct SQSs at the x = 0.125 composition. The dielectric response in **Figure 11** is shown in red for the [001] as this is the out of plane direction for the synthesized thin-film direction for which the dielectric constant is measured. There is a limited increase for one of the orderings at x = 0.0625, but otherwise no dielectric enhancement is predicted. The piezoelectric response of each unique ordering is shown in **Figure 11** as a blue x. In order to reproduce the properties of the solid solution we also average the values of the Born effective charges, internal strain tensors, and force constants from these three individual SQS orderings and all symmetrically equivalent sites as defined in the methods section before calculating the piezoelectric tensor. These results are shown separately from the direct DFT calculations in **Figure 11** as circles. At a composition of x = 0.0625 we see that the individual orderings produce a two-fold increase in the piezoelectric response. Similarly the piezoelectric response generated from an average of properties from these two orderings produces a response of 5.49 C/m^2. At the x = 0.125 composition, there is a modest increase in the piezoelectric response for all orderings. However, the piezoelectric response calculated from an average of Born effective charges, internal strain tensors and force constants of three SQSs at x = 0.125 demonstrates a piezoelectric response which is 174% that of the $Sr_2Nb_2O_7$ endpoint. These results are consistent with the approximation for enhanced piezoelectric response generated from the linear interpolation of aforementioned alloy properties shown in the background of **Figure 11** although the enhancement appears earlier than in the approximation. The enhancement in piezoelectric response was found to be most strongly associated with the force constants and internal strain tensors of the

Nb/V cation site and corresponding oxygen cage. In addition, we report that there are no dynamic instabilities at the gamma point for the calculated alloys when the force constants are averaged across their SQS orderings.

3.4 Experimental Results

Motivated by the DFT predictions, we synthesized and characterized 100 nm-300 nm-thick single-crystalline (001)-oriented $Sr_2Nb_{2-2x}V_{2x}O_7$ (x = 0, 0.05, 0.1) films on (110)-oriented $SrTiO_3$ substrates. 30-45 nm thick $La_{0.7}Sr_{0.3}MnO_3$ were used as bottom and top electrodes. All the synthesized heterostructures were single-crystalline as shown in the X-ray diffraction ($\theta - 2\theta$) line scans shown in **Figure 12a**. The parent compound $Sr_2Nb_2O_7$ was found to possess an orthorhombic crystal structure with $Cmc2_1$ space-group symmetry and lattice parameters as a = 3.933Å, b = 26.726Å, and c = 5.683Å. Considering the difference in ionic radii between V^{+5} and Nb^{+5} is small (∼15%), V^{+5} is expected to substitute Nb^{+5} in the parent compound $Sr_2Nb_2O_7$ in an isovalent manner. The structure was found to remain in the crystalline orthorhombic phase as a function of vanadium concentration as shown in **Figure 12a**. The thin-film heterostructures for $Sr_2Nb_{2-2x}V_{2x}O_7$ with x > 0.1 were found to be challenging to synthesize as a single phase solid solution owing to the film's tendency to decompose to the parent phases i.e., $Sr_2V_2O_7$ and $Sr_2Nb_2O_7$. Such observations are consistent with the prior studies for bulk ceramics and the current study's calculations for a thermodynamically stable solid solution alloy in **Figure 10c**.[59] In addition to structural characterization, electrical properties of the heterostructures were probed to obtain the dielectric constant of the synthesized compositions. The dielectric constant is measured along the [001] and is found to be 32, 42, and 37 for compositions with x= 0, 0.05, and 0.1 in **Figure 12b**. We note the enhancement of dielectric constants with vanadium alloying to

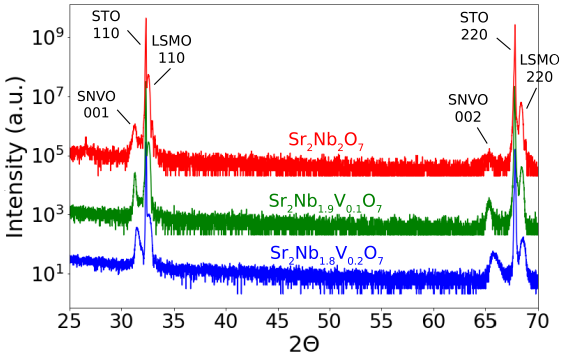

(a) XRD patterns of the $Sr_2Nb_{2-2x}V_{2x}O_7$ system.

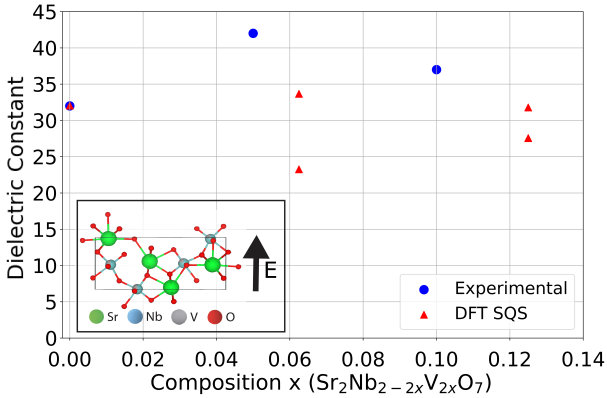

(b) Dielectric constant of the $Sr_2Nb_{2-2x}V_{2x}O_7$ system along the [001] compared to DFT calculations.

Figure 12: $Sr_2Nb_{2-2x}V_{2x}O_7$ alloys were synthesized epitaxially and characterized for crystal structure and dielectric properties

be promising for the polar properties of this alloy. While DFT results show no large enhancement of the dielectric properties with vanadium concentration along the [001], the discrepancy may be due to the epitaxial growth method introducing interfacial strains and limitations of DFT in modeling large unit cells.

3.5 Conclusion

Lead-free piezoelectric materials have been the subject of extensive research due to recent global regulations on lead.[1] Computational methods contribute a valuable tool to the high-throughput search for novel materials, especially outside of the traditional perovskite family. However, the exploration of MPBs, which comprise the majority of modern piezoelectric solutions, presents a number of technical challenges for computation. In this study, we first establish the ability of endpoint properties to provide a reasonable qualitative approximation for lattice dynamics in the PZT. We note that the exploration for softened phonon modes in this system correctly implies the presence of the tetragonal to rhombohedral MPB and presents an interesting potential descriptor for high-throughput MPB searches. We then examine the layered perovskite, $Sr_2Nb_2O_7$, as a parent compound and employ a Vegard's law-like approximation for exploring increased polar response based on the identification of softening phonon modes. A thorough screening of 19 potential cation substitutions for this compound was conducted to search for large piezoelectric response and thermodynamically stable solid solution alloys. From this screening, we identify $Sr_2Nb_{2-2x}V_{2x}O_7$ as a system with predicted enhanced piezoelectric and dielectric properties. We conduct an 88-atom unit cell calculation of the piezoelectric tensor of $Sr_2Nb_{2-2x}V_{2x}O_7$ at x = 0.0625 and 0.125 for multiple cation orderings at each composition and find a significant 184% enhanced piezoelectric response of this alloy due to softened phonon modes and a favorable change in the internal strain tensors. These DFT calculations also predicted slightly enhanced dielectric properties at the x = 0.0625 composition. This alloy was synthesized through pulsed-laser deposition and found to form a solid solution alloy with increased dielectric properties as a function of vanadium doping. Future work will determine the piezoelectric properties of this alloy as well as if the formation of an MPB may be possible. We present this alloy system as a promising lead-free piezoelectric material and this methodology as a screening tool for enhanced polar materials, especially with respect to potential MPB systems. We hope that this study allows for the high-throughput screening of piezoelectric alloy systems and the experimental discovery of lead-free material systems.

3.5.1 Completing the Materials Discovery Pipeline

During the course of this work to produce a successful pipeline from *ab initio* calculations to physically realized piezoelectric systems, many practical bottlenecks were encountered. Oftentimes, *ab initio* studies may fail to appropriately consider the effects of thermodynamic stability, defects, and magnetism, lowering the probability of forming the target structure or producing undesired phases.[63] In our study, phase segregation in $Sr_2Nb_{2-2x}V_{2x}O_7$ occurred past x = 0.15, which was suggested, but not specifically predicted by our thermodynamic

analysis. While our target composition was still synthesizeable, proper characterization of the sample presented another tedious step in the process of experimental validation. Attempts to synthesize novel structures can produce multi-phase samples in unexplored chemical spaces, requiring high-throughput characterization techniques.[64] We attempt to combat this specific characterization bottleneck by developing an automated XRD structure solution package to accelerate the materials discovery pipeline in the following work.

Chapter 4

Solving Inorganic Crystal Structures from X-ray Powder Diffraction Using a Generative First-Principles Framework

4.1 Introduction

X-ray powder diffraction (XRD) is a ubiquitous method for the characterization of crystal structures of inorganic materials. To solve a crystal structure from XRD, the diffraction pattern obtained from a sample is compared to reference patterns of structures from the target chemical space. Subsequently, the matching structure(s) can be further refined with techniques such as Rietveld refinement.[65] However, when a completely new crystal structure is encountered, the interpretation and subsequent solution of the structure from the XRD pattern may be time consuming and indeterminate even for domain experts.[66,67,68,69]

Several steps are needed to characterize a new inorganic crystal structure from experimental XRD patterns. First, the measured patterns may be processed to account for background, and to identify peak locations and intensities. Next, the lattice parameters and space group are identified. These first two steps of solving a crystal structure may be difficult when the XRD patterns are low resolution or the sample contains multiple phases. However, established figures of merit (M_{20}, F_N, WRIP20)[70,71,72], and multiple open source software programs have been developed to automate and clarify the unit cell classification process.[73,74]

The final, and often most challenging step is to determine the atomic positions within a unit cell. Reciprocal space methods can determine the crystal structure exactly, but are limited by peak overlap and resolution limits.[75] For most samples, especially those available in the form of microcrystalline powder, direct space approaches are generally more practical and widely used.[76,77,78,79] These techniques involve global optimization of free parameters describing the crystal structure, and utilize domain knowledge to reduce the available degrees of freedom as much as possible. Methods including simulated annealing, genetic algorithms, and particle swarm have all been used to deduce the atomic positions.[80,81,82,76,83,84] While these approaches have been shown to be effective in solving a wide range of crystal structures across chemistries, many rely on the specification of an expected structure or atomic building blocks such as oxygen tetrahedra or prototype structures to reduce the free parameters as much as possible.[80,81,82,84,83] In some cases, these heuristics can introduce a barrier by limiting relevant degrees of freedom or a bias by way of structure sampling which can influence the structure solution technique. In addition, this task may be especially difficult in less common chemical systems such as sulfides and nitrides, which are becoming fertile grounds for materials discovery.[85] To avoid these biases and limitations, methods utilizing structure

generation schemes such as CALYPSO do not place restraints on the starting symmetry.[82,86] However, this greatly expands the structural search space and complexity to all 230 space groups. FPASS, which implements a genetic algorithm, similarly generalizes the search space by parameterizing all degrees of freedom associated with the symmetry groups consistent with XRD.[76]

In this work, we introduce an automated, open-source Python framework for solving inorganic crystal structures by XRD, coupling systematic, exhaustive structure generation with first-principles density functional theory (DFT) simulations. Given an indexed XRD pattern, together with the associated lattice parameters, space group, and expected elemental composition, our Automated XRD to Structure (AXS) framework follows an efficient path that utilizes the symmetry operations of the space group and subsequent degrees of freedom to generate crystal structures which span the space of possible structures in the space group and chemical system. These structures are filtered to avoid atomic overlap, ranked based on their goodness-of-fit to the diffraction pattern, and then high-ranking structures are relaxed with DFT to obtain the optimal atomic positions while assessing energetic viability of the structure. This software is unique from other direct space approaches in that candidate structures span the constrained space of possible structures, sampling the search space with a user specified density. The AXS procedure is guaranteed to encompass the correct solution to a single phase inorganic crystalline XRD sample with known chemical composition as atomic positions are sampled on finer grids, and hence is improvable by increasing the computational budget. For this reason, we hope this methodology can be a benchmark for automated XRD structure solution in the future as computational power becomes more and more accessible. The success of direct space methods to solve crystal structures, including this one, is generally limited by the high dimensionality of the search space. However, the use of crystal symmetry, physically-motivated filter, and increased compute power allows for efficient structure generation. We demonstrate that AXS obtains the correct solution for 91 out of 99 structures under reasonable computational costs for both structure generation and DFT, and also use AXS to solve three light element containing crystal structures (one previously unsolved). We offer this algorithm as a basic framework for any user to solve crystal structure from XRD patterns as well as a proof of concept for brute force direct space structure solution framework to solve

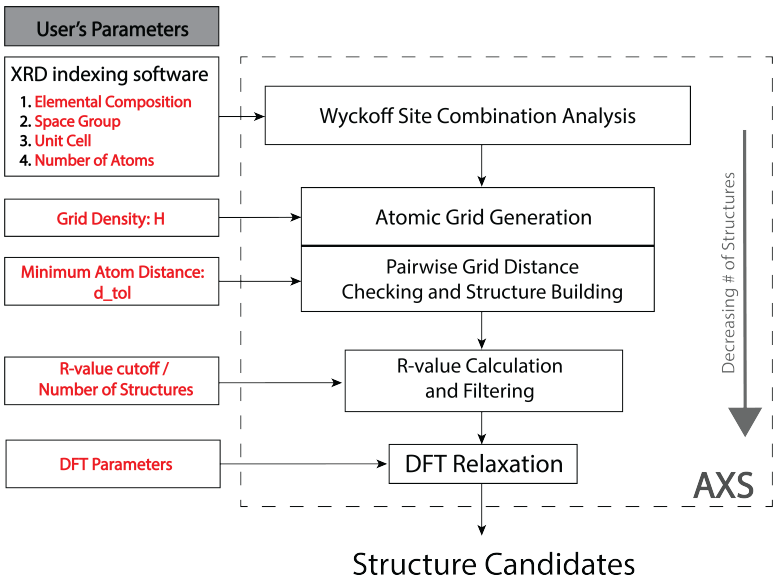

Figure 13: AXS Algorithm Flowchart

novel structures containing light elements from diffraction patterns.

4.3 Methodology

Our implementation of AXS takes an indexed XRD pattern as the starting point for the algorithm. Many reliable software packages for this indexing are widely available.[87] In addition, AXS expects the space group and unit cell parameters corresponding to the indexed pattern as input, as well as the chemical identity and number of atoms in the unit cell. A flowchart detailing the workflow is presented in **Figure 13**.

In the first step, AXS provides the Wyckoff positions of the input space group. As each Wyckoff site is associated with a certain multiplicity, there exist a finite number of combinations of Wyckoff sites possible for a specified chemical system and number of atoms. These combinations are enumerated and output by AXS, starting with those with the lowest number of unique Wyckoff sites. This order reflects the occupations of Wyckoff sites across experimental inorganic structures in the Inorganic Crystal Structure Database (ICSD)[88].

The user can then choose the Wyckoff site combinations from which to sample the structure space. As a default setting, the AXS algorithm includes all possible Wyckoff site combinations in the structure search. For each Wyckoff site combination that satisfies the atom count constraint, we attempt to consider all structures which satisfy the associated symmetry constraints. We generate the search space of Wyckoff positions by constraining candidate positions to lie on a 3-dimensional grid. Symmetrically equivalent positions associated with the candidate position are also generated. Each individual candidate position will therefore contain a number of atoms equal to the multiplicity of the special Wyckoff site. The grid density, `H`, is defined by the user in units of grid points per Å($\mathring{A}^{-1}$) and is the same in all three dimensions. These candidate atomic positions are generated for each Wyckoff position in the valid combination. These candidate positions, which span the degrees of freedom of each Wyckoff position at the user-specified density, are then compared pairwise against candidates of every other Wyckoff position to check for overlap in atomic positions. This collision tolerance parameter which defines atomic overlap, `d_tol`, is specified by the user. Once every individual candidate position is checked against all others candidates from distinct Wyckoff sites, we assemble all possible valid sets of candidate positions into structures which span the degrees of freedom of the Wyckoff sites.

Next, simulated XRD patterns for these structures are generated utilizing Pymatgen's XRD module.[89] These calculated candidate patterns are compared to the target XRD pattern of interest for closeness of fit which is done by minimizing the objective function:

$$R = \sum_{peaks} (I_t - I_c)^2 / \sum_{peaks} I_c \tag{20}$$

where I_c and I_t are the intensities of calculated candidate peaks and target peaks, respectively, and I_c peak values within 0.15° 2θ of each I_t peak are included in the sum. While we utilize indexed peak intensities in this work,[84,83] the AXS framework also includes the capability to compare to point intensities in whole XRD patterns (with an example in the

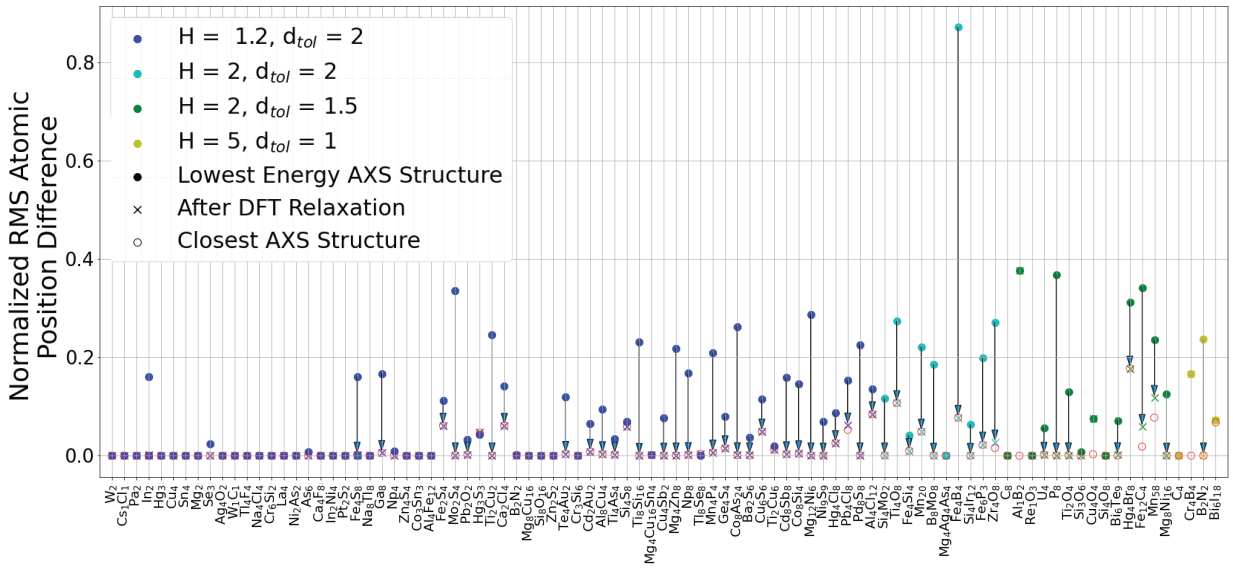

Figure 14: Normalized root mean square error of AXS structures relative to benchmark structures. The x's correspond to the lowest-energy DFT-optimized structure for each compound, and filled circles correspond to the same AXS candidate before DFT structural optimization. Empty red circles correspond to the optimized structure closest to the ground state structure as determined through DFT. Candidates obtained from an initial grid density of `H` = 1.2 Å^{-1} and `d_tol` = 2 Å are shown in blue, `H` = 2 Å^{-1} and `d_tol` = 2 Åin cyan, `H` = 2 Å^{-1} and `d_tol` = 1.5 Å in green, `H` = 5 Å^{-1} and `d_tol`= 1 Åin yellow.

Supplementary Materials). Such objective functions have been widely used in the direct space structure solution field, sometimes with modifications to optimize particular systems.[84,83,76]

Finally, the structures with minimal R-values are optimized with DFT, where the R-value cutoff, or number of structures to be relaxed, is chosen by the user. The DFT geometry optimization is conducted with fixed cell parameters using the Vienna Ab Initio Simulation Package (VASP)[11,12] with the PBE Generalized Gradient Approximation (GGA)[30] + U for the exchange-correlation functional, and numerical parameters consistent with the Open Quantum Materials Database (OQMD).[90] Here, DFT relaxation serves the critical role of a physics-based energy optimization of the atomic positions from the initial guesses which are assessed with the figure of merit in equation (A.3.2).

4.4 Results

4.4.1 Benchmarking Dataset

AXS is tested on a dataset of 99 structures and their simulated stick patterns. The dataset is composed of inorganic crystal structures that are in the Materials Project database, includes structures with distinct crystal symmetries and chemical compositions, and draws from all crystal systems except triclinic, with sizes ranging from between 1 and 58 atoms in the

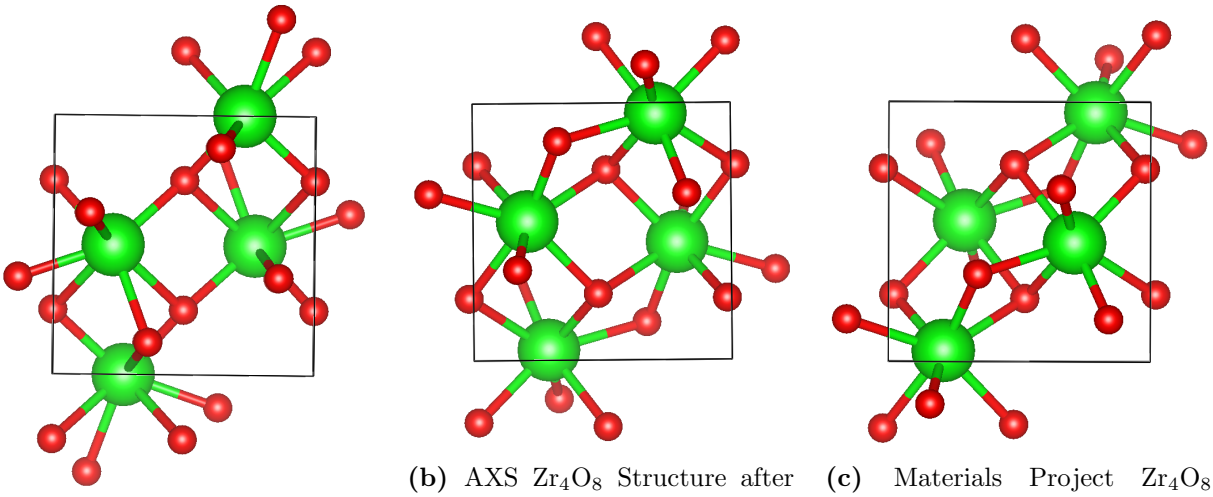

(a) Zr_4O_8 AXS Structure

(b) AXS Zr_4O_8 Structure after DFT Relaxation

(c) Materials Project Zr_4O_8 Structure

Figure 15: AXS produces a structure (a) at grid resolution (RMS = 0.271), which is then (b) relaxed using DFT (RMS = 0.027). These are shown compared to the ground state structure as determined through DFT (c). Structures are visualized using the VESTA software.[91]

primitive cell. This is the same dataset used for benchmarking a genetic algorithm based automated structure discovery method[88], with four larger structures added with greater than 30 atoms in the primitive cell. All structures in the dataset have corresponding entries in the ICSD, but lattice parameters and atomic positions used in generating the benchmark set stick patterns correspond to the DFT optimized structures.

Initial candidate structures are generated using a grid density `H` = 1.2 Å^{-1} and minimum atom distance `d_tol` = 2.0 Å. At this resolution, five compounds are found to have too large a configuration space for the AXS algorithm to be applied at reasonable computational cost. As a result, AXS "fails" for the following compounds: GeS_2 ($Fdd2$, 18 atoms in primitive cell), $CrCl_3$ ($P3_212$, 22 atoms in primitive cell), U_3Si ($I4/mcm$, 8 atoms in primitive cell), Se ($P2_1/c$, 32 atoms in primitive cell), and TiO_2 (Pbca, 24 atoms in primitive cell). After generating structures, filtering out structures with significant atomic overlap, and comparing XRD patterns, DFT structural optimization is performed for up to 50 candidates with the lowest R-values. This results in the correct solution for 63 compounds in the benchmark set. Here, correct structure solution is defined as finding the lowest-energy DFT structure calculated for a material to be within 0.2 root mean square distance in atomic positions relative to the correct structure, normalized by (Volume/Number of Sites)$^{1/3}$.

To assess the capabilities of AXS in the presence of greater computational resources, we systematically increase the resolution of the initial candidate set. At `H` = 2.0 Å^{-1} and `d_tol` = 2.0 Å, 10 additional structures are successfully solved; at `H` = 2.0 Å^{-1} and `d_tol` = 1.5 Å, 14 additional structures are successfully solved; and at `H` = 5.0 Å^{-1} and `d_tol` = 1.0 Å, 4 additional structures are solved. In total, the correct solution is found by AXS for 91 out of 99 of the structures in the dataset. These results are summarized in **Figure 14**. Apart

from the five compounds mentioned earlier, whose symmetries result in too large an initial configuration space, three additional structures (Cd_3I_6, Zr_3Si_8, and Nb_3S_6) are not solved by our AXS workflow. These structures are observed to have good structural matches within the initial generated structure space, but noise in the R-values leads to a deprioritization of these close-match structures when filtering before DFT calculations are performed.

In **Figure 15**, we show an example of a structure which is produced by AXS based on an XRD pattern from the ground state structure as determined from DFT. For this Zr_4O_8 ($P2_1/c$), the AXS algorithm calculates a total of 20 possible Wyckoff site configurations and takes 14.13 seconds to produce a total of 434 structures in spanning these configurations at a density of H = 2 $Å^{-1}$. XRD patterns for these structures are then calculated and compared to the experimental pattern according to equation (A.3.2), which takes 10.62 seconds. The lowest R-value structure proposed by AXS is then relaxed in DFT and is shown to nearly identical to that of the actual structure, taking 7458.25 seconds.

We would like to note that the production of XRD and calculation of R-values becomes the computationally limiting step of the AXS methodology for larger structure spaces. The time for diffraction pattern calculations and matching for each structure generated can be two orders of magnitude longer than the structure generation time, as shown in **Figure 16**.

In addition to the accuracy benchmarks, these results also allow us to analyze the dimensionality of the XRD structure solution problem. The total size of the structure search space corresponds to the number of initial set of candidate structures, which is computed

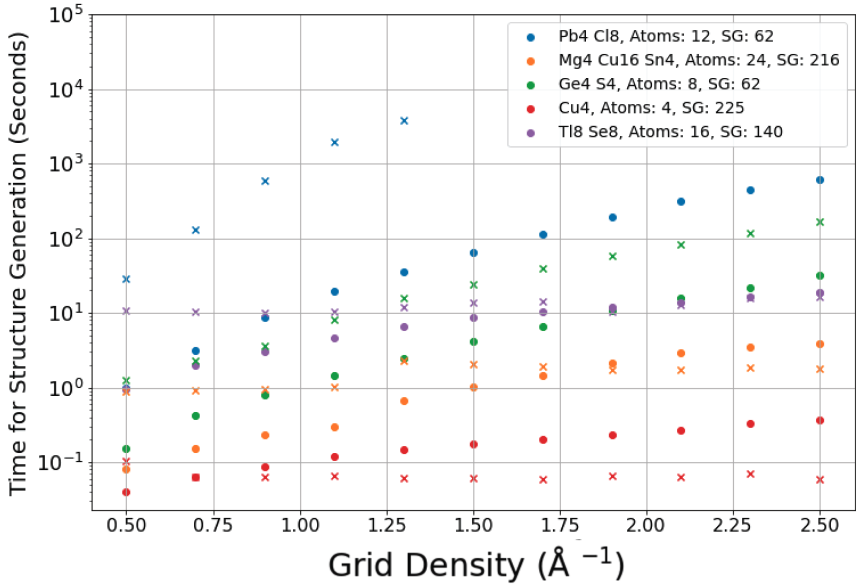

Figure 16: Timing benchmarks for structure generation (circles) and XRD pattern generation and R-value calculation (x's), for the AXS algorithm for structures of varying chemistries, space groups, and primitive cell sizes.

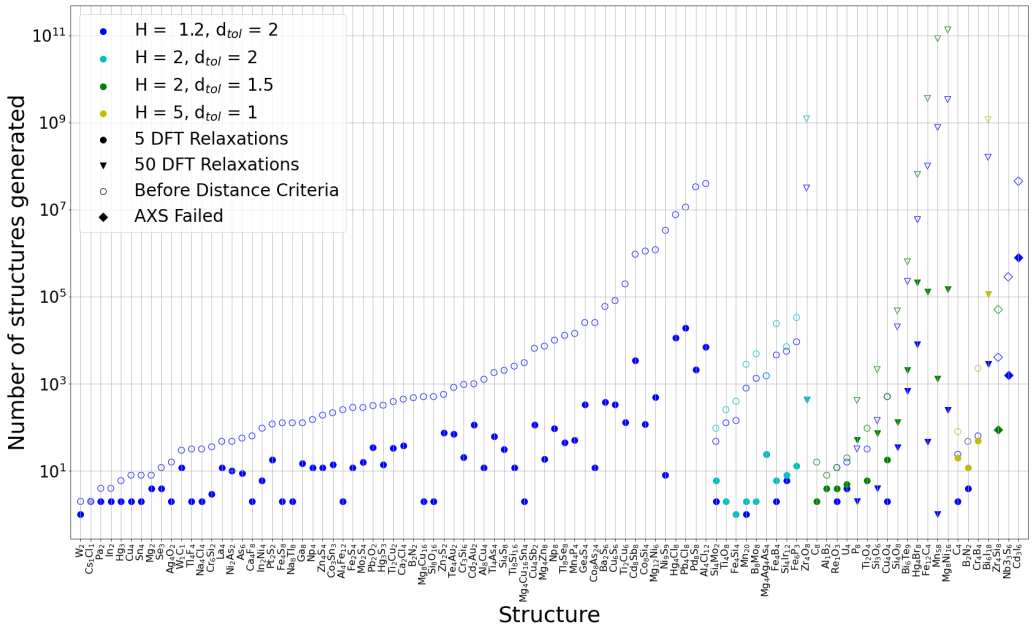

Figure 17: The number of structures AXS generates and filters at each step is shown for each compound. Color indicates the grid density and atom collision filtering parameters, unfilled markers indicate the initial full space of structures generated, and the shape indicates the number of structures optimized in DFT for final energy comparison.

with scaling no worse than number of atoms to sixth:

$$O(n) \propto \sum_{i \neq j} H^{DOF_i} * H^{DOF_j} \tag{21}$$

where the subscripts i and j refer to distinct Wyckoff sites and DOF indicated the degrees of freedom associated with each particular Wyckoff site. The scaling is proportional to the time required for atomic collision checks. For each Wyckoff site in a given structure, we generate grids spanning the asymmetric unit. These grids are checked against all of the grids in the other Wyckoff sites, leading to a time of $H^{DOF_i} * H^{DOF_j}$ for each pair of Wyckoff sites. In most cases, the scaling is better than exponential, but the scaling is poor for low symmetry space groups which contain low Wyckoff site multiplicities with a number of degrees of freedom. This can especially be seen in **Figure 16** for Ti_8Se_8 ($I4/mcm$), and Pb_4Cl_8 ($Pnma$).

For denser grids and for many space groups, this initial configuration space quickly becomes very large. However, with AXS we observe that the simple filtering mechanism of atomic overlap checking (via `d_tol`) can decrease the dimensionality of the search space by multiple orders of magnitude. This is illustrated in **Figure 17**, which shows the number of initial candidate structures generated across the benchmark set, as well as the number

of candidates considered at each step of the AXS workflow. At our default parameters of `H` = 1.2 Å^{-1} and `d_tol` = 2.0 Å, 41 compounds have fewer than 10 candidate structures even before R-value comparisons and filtering. This benchmark therefore demonstrates that the physically-relevant structure configuration space can actually be very small for certain materials, making the AXS algorithm a practical complement to structure solution algorithms that rely on optimization via machine learning, which target large configuration spaces.

4.4.2 Solving ICDD Structures

The AXS algorithm is also tested on experimental XRD patterns. While in the benchmarking dataset, the XRD patterns correspond exactly to DFT-optimized unit cells of known structure, this is not the case for experimental patterns. We use the AXS algorithm to solve the structure of three lithium containing compounds whose lattice parameters, space groups, and stick patterns are available in the Powder Diffraction File (PDF) from the International Centre for Diffraction Data (ICDD, 2021): Li_8HfO_6 (PDF 00-026-0847), Li_3CrO_4 (PDF 00-045-0347), and $LiFeO_2$ (PDF 00-052-0698).[92] Li_8HfO_6 (R-3) has been proposed to be isomorphic to Li_8ZrO_6,[93] and atomic positions have been solved for slightly different lattice parameters with POWD-12++ (PDF 04-022-5097).[71] Li_3CrO_4 ($Pmn2_1$) is thought to be isostructural to high temperature γ Li_3PO_4.[94] $LiFeO_2$ ($Pnma$) has no proposed structure solution. We choose `H` = 2 Å^{-1} and `d_tol` = 1.5 Å as structure search parameters. The atomic positions for the 100 structures with best-matching XRD patterns are optimized using DFT.

The energies of the DFT results are used to determine the stability of these theoretical structures and are shown in **Figure 18**. For Li_8HfO_6, we find a structure that is 0.005 eV/atom above the stability hull as defined in the Materials Project.[89] Interestingly, structures with slightly higher R-values in this space tend to relax to lower energy structures. The lowest R-value structures are caught in local minima demonstrating the importance of sampling a range of structures with low R-value. More dramatically for Li_3CrO_4, the AXS framework produces a structure which is 0.344 eV/atom below the stability hull as seen in **Figure 18c**. For the $LiFeO_2$ structure, AXS finds a structure which is approximately 0.0816 eV per atom below the hull after DFT relaxation with fixed lattice parameters. These structures, shown in **Figure 18b**, **Figure 18d**, and **Figure 18f**, represent previously unknown phases which lie near or below the energetic hull and qualitatively match the experimental powder diffraction patterns. In addition, the final Li_6HfO_8 structure found through the AXS algorithm is within a normalized RMS distance of 0.01 of the structure in the ICDD while the final Li_3CrO_4 structure is within a normalized RMS distance of 0.08 of the proposed isostructural Li_3PO_4 structure with a rescaled lattice. While it is uncertain if these represent the experimentally synthesized solutions of these compounds, the AXS algorithm has generated energetically plausible structures to be further analyzed. These structures are provided as CIF files in our Supplementary Materials.

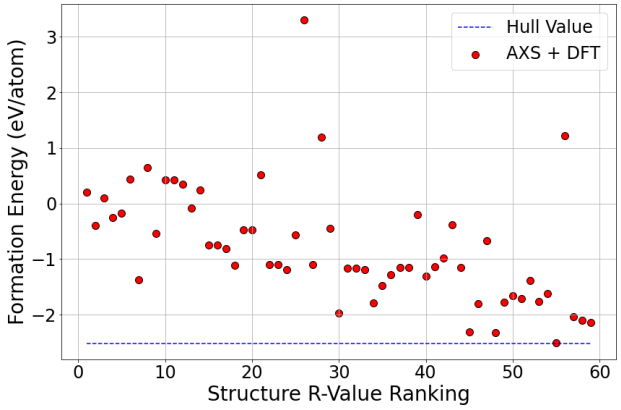

(a) Li_8HfO_6 AXS structure energies

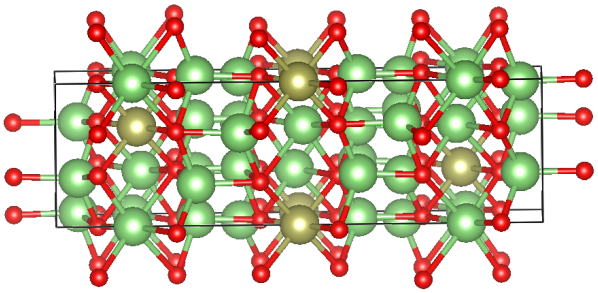

(b) Li_8HfO_6 Final AXS structure

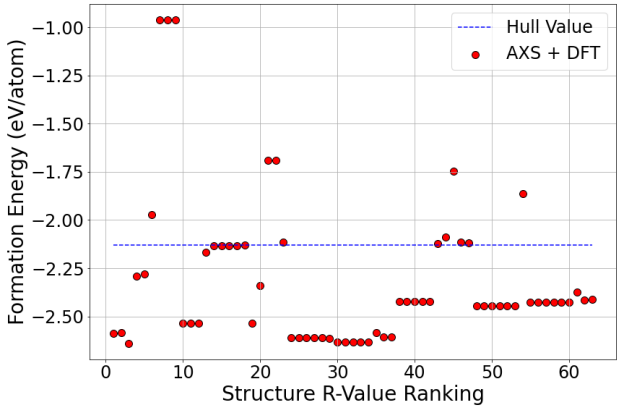

(c) Li_3CrO_4 AXS structure energies

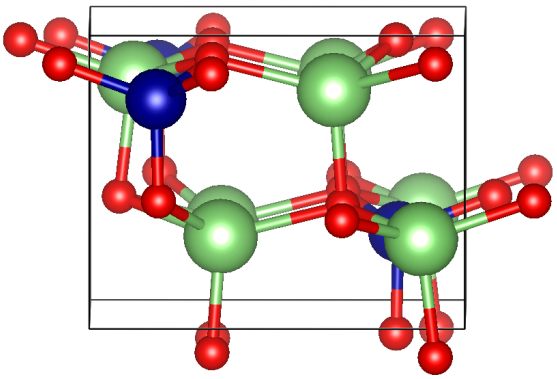

(d) Li_3CrO_4 Final AXS Structure

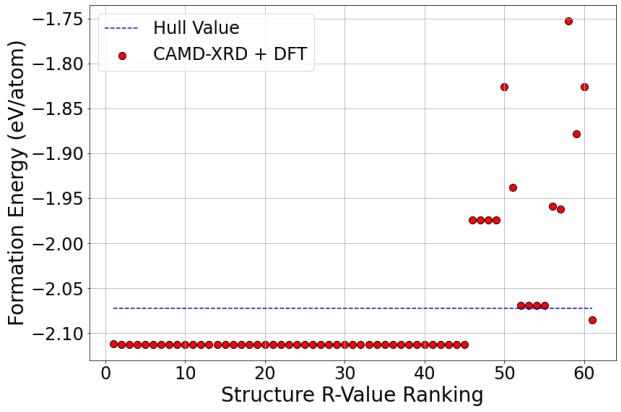

(e) $LiFeO_2$ AXS structure energies

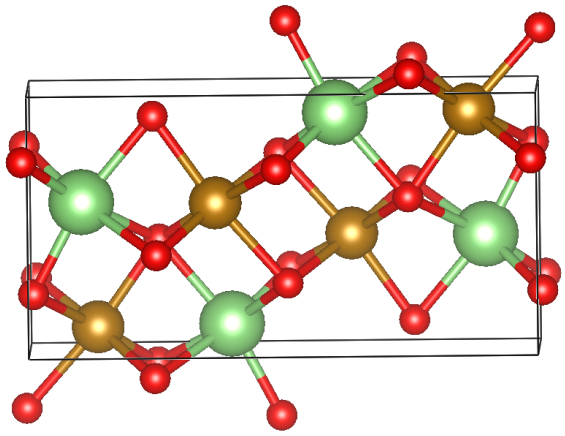

(f) $LiFeO_2$ Final AXS Structure

Figure 18: AXS proposes stable structures for Li_8HfO_6, Li_3CrO_4, and $LiFeO_2$ corresponding to XRD patterns from the ICDD.

4.5 Conclusion

Increasing computational power has allowed us to present AXS as an aid for the automatic, systematic, and efficient structure solution from XRD patterns in a completely agnostic manner. AXS exploits known crystal symmetries to tractably determine the large possible structure space for a given diffraction pattern. After generation of a spanning structure space and downsampling to eliminate atomic overlap, the best candidates are identified by first filtering by similarity of XRD patterns and then ranking by DFT-computed stability of the structure. We demonstrate the potential of AXS to determine the structure of compounds across a variety of compositions, symmetries, and cell sizes comparable to other automated structure solution algorithms with a 92% success rate. We hope AXS is not only useful as an automated XRD solution technique, but as a benchmark for further crystal structure solutions methods. While additional heuristics and advanced search algorithms may be added to this framework and other XRD solution software, AXS sets a reasonable standard for what is able to be accomplished through computational power and crystal symmetry alone. In addition, AXS is able to make advances in the structure solution of previously unsolved structures which are energetically stable. We present structures for $LiFeO_2$, Li_8HfO_6, and Li_3CrO_4 for further analysis and also to demonstrate the efficacy of this approach in providing viable structures to experimental crystal structures.

4.6 Data Availability

The code base for all analyses presented in this work is available at https://github.com/TRI-AMDD/CAMD-XRD.

Chapter 5
Conclusion and Future Work

5.1 Future Work

This work is aimed at understanding the design of piezoelectric alloys and accelerating materials discovery through computational frameworks. While this work provides greater understanding of the properties and computational methodologies required for analyzing promising piezoelectric material systems, further work would benefit the search for a suitable lead-free PZT replacement. A simple extension of the current study is to conduct more DFPT calculations on polar and ferroelectric materials in the Materials Project database. As of this work, there are approximately 3400 materials with these calculations available, many of which were conducted after our search for disorder-tolerant materials systems. The disorder-tolerance and alloy screening frameworks may then be used to target new alloyed materials systems for large piezoelectric response.

While our approximation of dynamic properties in alloys is a useful screening tool, additional computational work will be useful in better understanding the mechanism of piezoelectric enhancement in alloy systems. Our approximation of the dynamic properties provides insight into the instabilities which lead to low energy polarization rotation and large piezoelectric response. However, the current work assumes that the structures remain in a single phase and that the dynamic stability can be accessed before thermodynamic and dynamic driving forces produce defects or secondary phases. Furthermore, a softening of lattice dynamics is sufficient to produce enhanced polar response in computational studies while the large piezoelectric response in perovskite systems are also typically coupled to polarization rotation models.[4] PZT is particularly unique in that its MPB composition is able to sustain a three phase solid solution, each contributing unique degrees of freedom for the polarization direction. Therefore, in addition to our model which examines the phonon softening and thermodynamic stability of a single phase, it would be prudent to develop an approach which examines these properties for all metastable phases (especially polar phases) in the chemical system. A specific challenge of this approach lies in difficulty of identifying all relevant phases. Without a priori knowledge of the structure space, this is a challenging task, restricting the search to well traversed chemical systems. In addition, the temperature and unit cell limitations of DFT provide additional constraints for the precise modeling of room temperature solid solution phase competition. While cluster expansion models may be able to accurately capture the energies of disordered alloys, these techniques are computationally expensive and specific to a given material. Regardless, further analysis into the efficacy of computational methods in modeling multi-phase solid solution polar systems would be beneficial - perhaps benchmarking with the PZT system. In addition, continued collaborations with experimentalists are required to validate our framework for identifying promising piezoelectric systems. The piezoelectric response of the $Sr_2Nb_{2-2x}V_{2x}O_7$ system

must be determined throughout its composition space to help determine the limitations of our approach. This positive feedback loop between theoretical predictions and experimental validations is highly valuable to the materials discovery process. The presence, or lack thereof, of an MPB will be useful in the selection of additional calculations which will inform the experimental synthesis of new piezoelectric MPB systems.

Another crucial property responsible for the success of PZT, especially with respect to other perovskite systems, is its distinct temperature stable MPB. Therefore, in order to better understand suitable lead-free piezoelectric systems, it will be useful to consider the thermodynamic and dynamic stability of phases with respect to temperature. Temperature-dependent cluster expansion methods such as those developed by Reith et al.[95] may be used to determine the stability of solid solution phases with respect to one another. Again, computational expense is of concern, so this is likely best done as a later step in computational screening. Fitting these cluster expansion models to the rhombohedral, tetragonal, and monoclinic phases PZT would provide an interesting study on the ability of computational approaches to simulate the temperature-dependent properties of MPBs. The vibrational entropy of a structure may be obtained through the quasi-harmonic approximation[96]; however, the accuracy of this method may not be sufficient, especially around compositions near dynamic instabilities. Alternative methods to efficiently and accurately model solid solution phases around MPBs are necessary to incorporate finite temperature analysis into the computational search for lead-free piezoelectrics.

5.2 Conclusion

In this thesis, we explore the computational design of piezoelectric materials to find a lead-free replacement for PZT. It was found through analysis of the Materials Project database that the force constants, rather than the Born effective charges or internal strain tensor, control the deterioration of the piezoelectric response with respect to disorder. In addition, it is possible to qualitatively determine the magnitude of this deterioration in piezoelectric response by examining the lattice dynamic properties of a material. A multiple stable phonon mode criteria is developed to identify disorder-tolerant materials. This analysis led to a number of structures for which we were able to perform cation subsitutions and produce novel theoretical materials with large predicted piezoelectric response.

In order to capitalize on the piezoelectric systems suggested by the previous work, we designed a framework to explore the piezoelectric properties of solid solutions alloy systems. A Vegard's law-like linear interpolation of the Born effective charges, internal strain tensors, and force constants was utilized to reproduce the anomalous piezoelectric response of the PZT solid solution system. We noted, in particular, the ability of this approach to qualitatively capture the behavior of the lattice dynamics of PZT around the MPB. This approach was used to tractably explore all reasonable cation substitutions on promising candidate system, $Sr_2Nb_2O_7$, which arose from the search for disorder-tolerant materials. These approximations, in conjunction with an analysis of the thermodynamic metastabilty of the solid solution at intermediate alloy compositions allowed us to determine promising candi-

dates for cation substitution. The $Sr_2Nb_{2-2x}V_{2x}O_7$ system was identified to demonstrate predicted enhancement of the piezoelectric response as well as solid solution stability which were subsequently confirmed by large scale DFT calculations. $Sr_2Nb_{2-2x}V_{2x}O_7$ was synthesized through pulsed laser deposition and stable solid solution alloy was found up to x = 0.1 with enhanced dielectric properties as a function of vanadium concentration. This alloy system is presented as a promising piezoelectric for further study, and this methodology is offered as a framework for the identification of high performing piezoelectric alloys.

Finally, we present an auxiliary work on the development of an XRD structure solution package, Automated X-Ray Diffraction to Structure (AXS), to facilitate characterization at the end of the high-throughput materials discovery pipeline. We note that the AXS algorithm is unique in its approach which is guaranteed to encompass the correct structure solution given correct XRD indexing and sufficient sampling, and hence is improvable by increasing the computational budget. This package is shown to be robust across a benchmarking dataset of 99 structures diverse in chemical composition, crystal symmetry, and size, solving 92% of structures. In addition, AXS is utilized to successfully predict structure solutions for three light element experimental systems which may be difficult to characterize utilizing traditional XRD solution techniques: $LiFeO_2$, Li_8HfO_6, and Li_3CrO_4. We provide this package as a tool for the automated solution of indexed XRD patterns, and hope that it is particularly useful for accelerating materials discovery and the high-throughput characterization of materials systems.

References

[1] Andrew J Bell and Otmar Deubzer. "Lead-free piezoelectrics—The environmental and regulatory issues". In: *MRS Bulletin* 43.8 (2018), pp. 581–587. DOI: 10.1557/mrs.2018.154.

[2] Gen Shirane, Kazuo Suzuki, and Akitsu Takeda. "Phase transitions in solid solutions of PbZrO3 and PbTiO3 (II) X-ray study". In: *Journal of the Physical Society of Japan* 7.1 (1952), pp. 12–18.

[3] B Jaffe, R S Roth, and S Marzullo. "Piezoelectric properties of lead zirconate-lead titanate solid-solution ceramics". In: *Journal of Applied Physics* 25.6 (1954), pp. 809–810.

[4] P. K. Panda and B. Sahoo. "PZT to lead free piezo ceramics: A review". In: *Ferroelectrics* 474.1 (2015), pp. 128–143. ISSN: 15635112. DOI: 10.1080/00150193.2015.997146.

[5] Xavier Gonze. "Adiabatic density-functional perturbation theory". In: *Physical Review A* 52.2 (1995).

[6] Stefano Baroni et al. "Green's-Function Approach to Linear Response in Solids Stefano". In: *Physical Review Letters* 58.18 (1987), pp. 1861–1864.

[7] R M Sternheimer. "Electronic polarizabilities of ions from the Hartree-Fock wave functions". In: *Physical Review* 96.4 (1954), p. 951.

[8] Xavier Gonze and Changyol Lee. "Dynamical matrices, Born effective charges, dielectric permittivity tensors, and interatomic force constants from density-functional perturbation theory". In: *Physical Review B* 55.16 (1997), p. 10355.

[9] Xavier Gonze and J-P Vigneron. "Density-functional approach to nonlinear-response coefficients of solids". In: *Physical Review B* 39.18 (1989), p. 13120.

[10] Xifan Wu, David Vanderbilt, and D. R. Hamann. "Systematic treatment of displacements, strains, and electric fields in density-functional perturbation theory". In: *Physical Review B - Condensed Matter and Materials Physics* 72.3 (2005). ISSN: 10980121. DOI: 10.1103/PhysRevB.72.035105. arXiv: 0501548 [cond-mat].

[11] G. Kresse and J. Hafner. "Ab initio molecular dynamcis for liquid metals". In: *Physical Review B* 47.1 (1993), p. 558. ISSN: 0163-1829. DOI: 10.1103/PhysRevB.47.558. arXiv: 0927-0256(96)00008 [10.1016]. URL: https://journals.aps.org/prb/pdf/10.1103/PhysRevB.47.558.

[12] G Kresse and J Furthmu. "<vasp26-PhysRevB.54.11169.pdf>". In: 54.16 (1996). ISSN: 03759393. DOI: 10.1103/PhysRevB.54.11169. arXiv: 0927-0256(96)00008 [10.1016].

[13] Paul Peter Ewald. "Zur begründung der kristalloptik". In: *Annalen der Physik* 359.24 (1917), pp. 557–597.

[14] Warren E Pickett. “Pseudopotential methods in condensed matter applications”. In: *Computer Physics Reports* 9.3 (1989), pp. 115–197.

[15] Jie Xing et al. “Properties and structures of nonstoichiometric (K, Na)NbO3-based lead-free ceramics”. In: *Journal of the American Ceramic Society* 101.4 (2018), pp. 1632–1645. ISSN: 15512916. DOI: 10.1111/jace.15326.

[16] Y Saito et al. “”Lead-free piezoceramics””. In: *Nature* 432.7013 (2004), pp. 84–87. ISSN: 0028-0836. DOI: 10.1038/nature03008.1..

[17] Jing Feng Li et al. “(K, Na) NbO3-based lead-free piezoceramics: Fundamental aspects, processing technologies, and remaining challenges”. In: *Journal of the American Ceramic Society* 96.12 (2013), pp. 3677–3696. ISSN: 00027820. DOI: 10.1111/jace.12715.

[18] Bao Quan Ming et al. “Piezoelectric properties of (Li, Sb, Ta) modified (Na,K) NbO3 lead-free ceramics”. In: *Journal of Applied Physics* 101.5 (2007). ISSN: 00218979. DOI: 10.1063/1.2436923.

[19] Shujun Zhang, Ru Xia, and Thomas R Shrout. “Modified based lead-free piezoelectrics with broad temperature usage range”. In: *Applied Physics Letters* 132913 (2007), pp. 2005–2008. DOI: 10.1063/1.2794400.

[20] Na Tio et al. “Enhanced ferroelectric properties and thermal stability of Mn-doped 0.96(Bi0.5 Na0.5)TiO3-0.04BiAlO3 ceramics”. In: *Journal of the American Ceramic Society* October 2016 (2017), pp. 1030–1036. DOI: 10.1111/jace.14645.

[21] Ting Zheng and Jiagang Wu. “Effects of site engineering and doped element types on piezoelectric and dielectric properties of bismuth ferrite lead-free ceramics”. In: *Journal of Materials Chemistry C* (2015), pp. 15–19. DOI: 10.1039/c5tc02203g.

[22] C Tholander et al. “Large piezoelectric response of quarternary wurtzite nitride alloys and its physical origin from first principles”. In: *Physical Review* 174119.92 (2015). DOI: 10.1103/PhysRevB.92.174119.

[23] Zhi Tan et al. “Intrinsic origin of enhanced piezoelectricity in alkali niobate - based lead - free ceramics”. In: *Journal of the American Ceramic Society* January 2019 (2019), pp. 5262–5270. DOI: 10.1111/jace.16365.

[24] B Akgenc et al. “First e principles calculations on stability and mechanical properties of various ABO 3 and their alloys”. In: *Materials Chemistry and Physics* 205 (2018), pp. 315–324. ISSN: 0254-0584. DOI: 10.1016/j.matchemphys.2017.11.026. URL: https://doi.org/10.1016/j.matchemphys.2017.11.026.

[25] L Hultman et al. “Ab initio calculations and experimental study of piezoelectric YxIn1-xN thin films deposited using reactive magnetron sputter epitaxy”. In: *Acta Materialia* 105 (2016), pp. 199–206. DOI: 10.1016/j.actamat.2015.11.050.

[26] Kenji Hirata et al. “First-Principles Study of Piezoelectric Properties and Bonding Analysis in (Mg , X , Al) N Solid Solutions (X = Nb , Ti , Zr , Hf)”. In: *ACS Omega* 4 (2019), pp. 15081–15086. ISSN: 2470-1343. DOI: 10.1021/acsomega.9b01912.

[27] P Daoust, P Desjardins, and R A Masut. "Ab initio piezoelectric properties of Al0.5Sc0.5N : Impact of alloy configuration on the d33,f piezoelectric strain coefficient". In: *Physical Review Materials* 055402 (2017), pp. 3–7. DOI: 10.1103/PhysRevMaterials.1.055402.

[28] Maarten de Jong et al. "A database to enable discovery and design of piezoelectric materials". In: *Scientific Data* 2 (2015), p. 150053. ISSN: 2052-4463. DOI: 10.1038/sdata.2015.53. URL: http://www.nature.com/articles/sdata201553.

[29] Stefano Baroni et al. "Phonons and related crystal properties from density-functional perturbation theory". In: *REVIEWS OF MODERN PHYSICS* 73 (2001).

[30] John P Perdew, Kieron Burke, and Matthias Ernzerhof. "Generalized Gradient Approximation Made Simple John". In: *Physical Review Letters* 77.18 (1996), pp. 3865–3868. ISSN: 0031-9007. DOI: 10.1103/PhysRevLett.77.3865. arXiv: 0927-0256(96)00008 [10.1016].

[31] Eran Bouchbinder and Edan Lerner. "Universal disorder-induced broadening of phonon bands : from disordered lattices to glasses Universal disorder-induced broadening of phonon bands : from disordered lattices to glasses". In: *New Journal of Physics* (2018), pp. 0–16.

[32] Claudia Bungaro and K M Rabe. "Lattice instabilities of PbZrO3 PbTiO3 superlattices from first principles". In: *Physical Review B* 65.January (2002), pp. 1–9. DOI: 10.1103/PhysRevB.65.224106.

[33] Fritz Körmann et al. "Phonon broadening in high entropy alloys". In: *npj Computational Materials* April (2017), pp. 1–8. ISSN: 2057-3960. DOI: 10.1038/s41524-017-0037-8. URL: http://dx.doi.org/10.1038/s41524-017-0037-8.

[34] Atsushi Togo and Isao Tanaka. "Scripta Materialia First principles phonon calculations in materials science". In: *Scripta Materialia* 108 (2015), pp. 1–5. ISSN: 1359-6462. DOI: 10.1016/j.scriptamat.2015.07.021. URL: http://dx.doi.org/10.1016/j.scriptamat.2015.07.021.

[35] Shi Erwei Xin Jun, Zheng Yanqing. "Piezoelectricity of zinc-blende and wurtzite structure binary compounds". In: *Applied Physics Letters* 112902 (2007), p. 91. DOI: 10.1063/1.2783279.

[36] R R Neurgaonkar et al. "Piezoelectricity in tungsten bronze crystals". In: *Ferroelectrics* 160.1563-5112 (1994), pp. 265–276.

[37] Ting Zheng et al. "Progress in Materials Science Recent development in lead-free perovskite piezoelectric bulk materials". In: *Progress in Materials Science* 98.January (2018), pp. 552–624. ISSN: 0079-6425. DOI: 10.1016/j.pmatsci.2018.06.002. URL: https://doi.org/10.1016/j.pmatsci.2018.06.002.

[38] J L Soubeyroux, Laboratoire De Chirnie, and Talence Cedex. "ETUDE PAR DIFFRACTION NEUTRONIQUE DES SOLUTIONS SOLIDES Kl _ xBixFl + 2x ET Rbl _ xBixFl + 2x". In: *Solid State Ionics* 6 (1982), pp. 103–111.

[39] T Vogt. "Neutron Powder Investigation Fluoride Solid Solutions of Praseodymium and Cerium Nitride". In: *Journal of Solid State Chemistry* 83 (1989), pp. 324–331.

[40] Muratahan Aykol et al. "Thermodynamic limit for synthesis of metastable inorganic materials". In: *Science Advances* April (2018), pp. 1–8.

[41] R Woods-Robinson et al. "The role of disorder in the synthesis of metastable ternary nitrides. arXiv 2020". In: *arxiv* (2020).

[42] Dragan Damjanovic. "Contributions to the Piezoelectric Effect in Ferroelectric Single Crystals and Ceramics". In: *Journal of the American Ceramic Society* 2676 (2005). DOI: 10.1111/j.1551-2916.2005.00671.x.

[43] Hyeong Jae Lee et al. "High Temperature, High Power Piezoelectric Composite Transducers". In: *Sensors (Basel, Switzerland)* 14 (2014), pp. 14526–14552. DOI: 10.3390/s140814526.

[44] Rickard Armiento et al. "Screening for high-performance piezoelectrics using high-throughput density functional theory". In: *Physical Review B* 014103 (2011), pp. 1–13. DOI: 10.1103/PhysRevB.84.014103.

[45] R Armiento et al. "High-throughput screening of perovskite alloys for piezoelectric performance and thermodynamic stability". In: *Physical Review B* 134103 (2014), pp. 1–9. DOI: 10.1103/PhysRevB.89.134103.

[46] Xiaoning Jiang et al. "High-Temperature Piezoelectric Sensing". In: *Sensors* (2014), pp. 144–169. DOI: 10.3390/s140100144.

[47] Ioannis Petousis et al. "Data Descriptor: High-throughput screening of inorganic compounds for the discovery of novel dielectric and optical materials". In: *Scientific Data* 4 (2017), pp. 1–12. ISSN: 20524463. DOI: 10.1038/sdata.2016.134.

[48] Y. Murakami N. Nakanishi, A. Nagasawa. "LATTICE STABILITY AND SOFT MODES". In: *Journal de Physique Colloques* 43 (1982), pp. C4–35–C4–55. DOI: <10.1051/jphyscol:1982403>.<jpa-00221947>.

[49] Izumi Tomeno et al. "Simultaneous softening of acoustic and optical modes in cubic PbTiO 3". In: *Physical Review B - Condensed Matter and Materials Physics* 86.13 (2012), pp. 1–15. ISSN: 1550235X. DOI: 10.1103/PhysRevB.86.134306.

[50] Yi Wang et al. "Phonon dispersions in random alloys : a method based on special quasi-random structure force constants". In: (2011). DOI: 10.1088/0953-8984/23/48/485403.

[51] M Asta. "Transferable force-constant modeling of vibrational thermodynamic properties in fcc-based Al-". In: *Physical Review B* (2007), pp. 1–15. DOI: 10.1103/PhysRevB.75.104117.

[52] Fei Zhou et al. "Compressive sensing lattice dynamics. I. General formalism". In: *arXiv:1805.08904v3* (2019), pp. 1–39. arXiv: arXiv:1805.08904v3.

[53] Fredrik Eriksson, Erik Fransson, and Paul Erhart. "The Hiphive Package for the Extraction of High-Order Force Constants by Machine Learning". In: *Advanced Theory and Simulations* 2.5 (2019), pp. 1–11. ISSN: 25130390. DOI: 10.1002/adts.201800184.

[54] Brian K. Voas et al. "Special quasirandom structures to study the (K0.5Na0.5)Nb O3 random alloy". In: *Physical Review B - Condensed Matter and Materials Physics* 90.2 (2014), pp. 1–6. ISSN: 1550235X. DOI: 10.1103/PhysRevB.90.024105.

[55] Handong Ling, Shyam S Dwaraknath, and Kristin A Persson. "Origin of Disorder Tolerance in Piezoelectric Materials and Design of Polar Systems". In: *Chemistry of Materials* (2020). DOI: 10.1021/acs.chemmater.9b04614.

[56] Huanpo Ning, Haixue Yan, and Michael J Reece. "Piezoelectric Strontium Niobate and Calcium Niobate Ceramics with". In: *Journal of the American Ceramic Society* 1413.26719 (2010), pp. 1409–1413. DOI: 10.1111/j.1551-2916.2009.03587.x.

[57] Lizhen Zhang et al. "From Sr 2 Nb 2 O 7 to Ca x Sr 2 x Nb 2 O 7 : An E ff ective Enhancement of Nonlinear Optical Activity by a Simple Way of Cation Substituting". In: *Crystal Growth and Design* (2018). DOI: 10.1021/acs.cgd.8b00584.

[58] Zhipeng Gao et al. "The Effect of Barium Substitution on the Ferroelectric Properties of Sr 2 Nb 2 O 7 Ceramics". In: *Journal of the American Ceramic Society* 1170.31993 (2013), pp. 1163–1170. DOI: 10.1111/jace.12121.

[59] Seana Seraji et al. "Processing and properties of vanadium doped strontium niobate". In: *Materials Science and Engineering: B* 88.1 (2002), pp. 73–78. ISSN: 0921-5107. DOI: 10.1016/S0921-5107(01)00909-6.

[60] Atsushi Honda, Li Shi-chang, and Zheng Yuan-lei. "First principles study on lattice vibration and electrical properties of layered perovskite Sr 2 x 2 O 7 (x = Nb , Ta)". In: *Chinese Physics B* 27 (2018). DOI: 10.1088/1674-1056/27/8/086104.

[61] A van de Walle, M Asta, and G Ceder. "The alloy theoretic automated toolkit: A user guide". In: *Calphad* 26.4 (2002), pp. 539–553. ISSN: 0364-5916. DOI: https://doi.org/10.1016/S0364-5916(02)80006-2. URL: http://www.sciencedirect.com/science/article/pii/S0364591602800062.

[62] H Jaffe and D A Berlincourt. "Piezoelectric transducer materials". In: *Proceedings of the IEEE* 53.10 (1965), pp. 1372–1386.

[63] Alex Zunger. *Beware of plausible predictions of fantasy materials*. 2019.

[64] Alfred Ludwig. "Discovery of new materials using combinatorial synthesis and high-throughput characterization of thin-film materials libraries combined with computational methods". In: *NPJ Computational Materials* 5.1 (2019), pp. 1–7.

[65] H M Rietveld. "A profile refinement method for nuclear and magnetic structures". In: *Journal of Applied Crystallography* 2.2 (1969), pp. 65–71. DOI: 10.1107/S0021889869006558. URL: https://doi.org/10.1107/S0021889869006558.

[66] B D Cullity and Stuart Stock. *Elements of X-ray Diffraction*. Upper Saddle River, 2001.

[67] Radovan Černý. "Crystal structures from powder diffraction: Principles, difficulties and progress". In: *Crystals* 7.5 (2017). ISSN: 20734352. DOI: 10.3390/cryst7050142.

[68] V K Pecharsky and P Y Zavalij. *Fundamentals of Powder Diffraction and Structural Characterization of Materials*. Boston, MA: Springer US, 2009. ISBN: 978-0-387-09578-3. DOI: 10.1007/978-0-387-09579-0. URL: http://link.springer.com/10.1007/978-0-387-09579-0.

[69] Luca Lutterotti et al. "Full-profile search–match by the Rietveld method". In: *Journal of Applied Crystallography* 52.3 (2019), pp. 587–598. ISSN: 16005767. DOI: 10.1107/S160057671900342X.

[70] P M de de Wolff. "A simplified criterion for the reliability of a powder pattern indexing". In: *Journal of Applied Crystallography* 1.2 (1968), pp. 108–113.

[71] G S Smith and R L Snyder. "FN: A criterion for rating powder diffraction patterns and evaluating the reliability of powder-pattern indexing". In: *Journal of Applied Crystallography* 12.1 (1979), pp. 60–65. DOI: 10.1107/S002188987901178X. URL: https://doi.org/10.1107/S002188987901178X.

[72] Angela Altomare et al. "Advances in powder diffraction pattern indexing: {\it N-TREOR09}". In: *Journal of Applied Crystallography* 42.5 (2009), pp. 768–775. DOI: 10.1107/S0021889809025503. URL: https://doi.org/10.1107/S0021889809025503.

[73] A Altomare et al. "Software packages for indexing and examples of their use". In: (2019).

[74] Radovan Černý and Vincent Favre-Nicolin. " FOX : A friendly tool to solve nonmolecular structures from powder diffraction ". In: *Powder Diffraction* 20.4 (2005), pp. 359–365. ISSN: 0885-7156. DOI: 10.1154/1.2135314.

[75] Werner Massa and Robert O Gould. "Crystal structure determination". In: (2004).

[76] Bryce Meredig and C Wolverton. "A hybrid computational–experimental approach for automated crystal structure solution". In: *Nature materials* 12.2 (2013), pp. 123–127.

[77] Kenneth D.M. Harris et al. "Crystal Structure Determination from Powder Diffraction Data by Monte Carlo Methods". In: *Journal of the American Chemical Society* 116.8 (1994), pp. 3543–3547. ISSN: 15205126. DOI: 10.1021/ja00087a047.

[78] G E Engel et al. "PowderSolve–a complete package for crystal structure solution from powder diffraction patterns". In: *Journal of applied crystallography* 32.6 (1999), pp. 1169–1179.

[79] Kenneth D M Harris and Eugene Y Cheung. "How to determine structures when single crystals cannot be grown: opportunities for structure determination of molecular materials using powder diffraction data". In: *Chemical Society Reviews* 33.8 (2004), pp. 526–538.

[80] M W Deem and J M Newsam. "Determination of 4-connected framework crystal structures by simulated annealing". In: *Nature* 342.6247 (1989), pp. 260–262. ISSN: 1476-4687. DOI: 10.1038/342260a0. URL: https://doi.org/10.1038/342260a0.

[81] Benson M. Kariuki et al. "The application of a genetic algorithm for solving crystal structures from powder diffraction data". In: *Chemical Physics Letters* 280.3-4 (1997), pp. 189–195. ISSN: 00092614. DOI: 10.1016/S0009-2614(97)01156-1.

[82] Pengyue Gao et al. "X-ray diffraction data-assisted structure searches". In: *Computer Physics Communications* 213 (2017), pp. 40–45. ISSN: 0010-4655. DOI: https://doi.org/10.1016/j.cpc.2016.11.007. URL: https://www.sciencedirect.com/science/article/pii/S0010465516303617.

[83] Angela Altomare et al. "The hybrid big bang{–}big crunch method for solving crystal structure from powder diffraction data". In: *Journal of Applied Crystallography* 46.3 (2013), pp. 779–787. DOI: 10.1107/S0021889813010571. URL: https://doi.org/10.1107/S0021889813010571.

[84] Vincent Favre-Nicolin and Radovan Černý. "{\it FOX}, 'free objects for crystallography': a modular approach to {\it ab initio} structure determination from powder diffraction". In: *Journal of Applied Crystallography* 35.6 (2002), pp. 734–743. DOI: 10.1107/S0021889802015236. URL: https://doi.org/10.1107/S0021889802015236.

[85] Wenhao Sun et al. "A map of the inorganic ternary metal nitrides". In: *Nature Materials* 18.7 (2019), pp. 732–739. ISSN: 1476-4660. DOI: 10.1038/s41563-019-0396-2. URL: https://doi.org/10.1038/s41563-019-0396-2.

[86] Yanchao Wang et al. "CALYPSO: A method for crystal structure prediction". In: *Computer Physics Communications* 183.10 (2012), pp. 2063–2070.

[87] Angela Altomare et al. "EXPO software for solving crystal structures by powder diffraction data: methods and application". In: *Crystal Research and Technology* 50.9-10 (2015), pp. 737–742.

[88] Logan Ward, Kyle Michel, and Chris Wolverton. "Automated crystal structure solution from powder diffraction data: Validation of the first-principles-assisted structure solution method". In: *Physical Review Materials* 1.6 (2017), pp. 1–13. ISSN: 24759953. DOI: 10.1103/PhysRevMaterials.1.063802.

[89] Shyue Ping Ong et al. "Python Materials Genomics (pymatgen): A robust, open-source python library for materials analysis". In: *Computational Materials Science* 68 (2013), pp. 314–319. ISSN: 0927-0256. DOI: https://doi.org/10.1016/j.commatsci.2012.10.028. URL: https://www.sciencedirect.com/science/article/pii/S0927025612006295.

[90] Scott Kirklin et al. "The Open Quantum Materials Database (OQMD): assessing the accuracy of DFT formation energies". In: *npj Computational Materials* 1.1 (2015), p. 15010. ISSN: 2057-3960. DOI: 10.1038/npjcompumats.2015.10. URL: https://doi.org/10.1038/npjcompumats.2015.10.

[91] Koichi Momma and Fujio Izumi. "{\it VESTA3} for three-dimensional visualization of crystal, volumetric and morphology data". In: *Journal of Applied Crystallography* 44.6 (2011), pp. 1272–1276. DOI: 10.1107/S0021889811038970. URL: https://doi.org/10.1107/S0021889811038970.

[92] Stacy Gates-Rector and Thomas Blanton. "The powder diffraction file: a quality materials characterization database". In: *Powder Diffraction* 34.4 (2019), pp. 352–360.

[93] J Hauck. "Über Lithiumhexaoxometallate". In: *Zeitschrift für Naturforschung B* 24.8 (1969), pp. 1067–1068.

[94] MAKL Dissanayake et al. "Synthesis and properties of a new $\beta$$polymorphofLi3CrO4". In: *Journal of Materials Chemistry* 4.8 (1994), pp. 1307–1308.

[95] D Reith et al. "First-principles modeling of temperature-and concentration-dependent solubility in the phase-separating alloy Fe x Cu 1- x". In: *Physical Review B* 86.2 (2012), p. 20201.

[96] Atsushi Togo and Isao Tanaka. "First principles phonon calculations in materials science". In: *Scripta Materialia* 108 (2015), pp. 1–5. ISSN: 1359-6462. DOI: https://doi.org/10.1016/j.scriptamat.2015.07.021. URL: https://www.sciencedirect.com/science/article/pii/S1359646215003127.

A Appendix

A.1 Additional Details for Chapter 2

Symmetry Constraints

The internal strain tensor is a Nx3x3x3 tensor in which N refers to each atomic site. Each of the 3x3x3 tensors must obey the point group symmetry of the atomic site as well as the symmetry operations which map equivalent atoms on to each other. The Born effective charges are similarly Nx3x3 matrices where each of the N 3x3 matrices must obey the point group symmetries centered around that site and equivalent atom mapping symmetry operations. However the Born effective charges also necessitate that a sum rule must be obeyed in order to respect the translational symmetry of the crystal:

$$\sum_m Z_m = 0 \tag{A.1.1}$$

The force constant matrix is a NxNx3x3 matrix in which N refers to the number of atomic sites in the unit cell. In this case, only the point group operations shared by both of the indexed atomic sites must be obeyed by each 3x3 matrix. In the same way, the atomic mapping operations must map pairs of atoms to equivalent pairs. Furthermore, two physical constraints must be considered. Similar to the Born effective charges, the force constant matrix must obey a corresponding acoustic sum rule in order to respect the translational symmetry of the crystal. Thus, the reciprocal space representation of the force constant matrix, the dynamical matrix, must obey the sum rule:

$$\sum_m C_{mi,nj} = 0 \tag{A.1.2}$$

Finally, the eigenvalues of the dynamical matrix must be positive. The eigenvalues represent phonon frequencies and negative values would suggest an imaginary phonon modes - instabilities in the lattice that indicate the preference for a new symmetry. Negative eigenvalues are randomly assigned a positive value and the acoustic sum rule is again enforced. These two rules are iteratively applied until both constraints are obeyed. A diagram of the algorithm is included in figure A.1.6

Figures

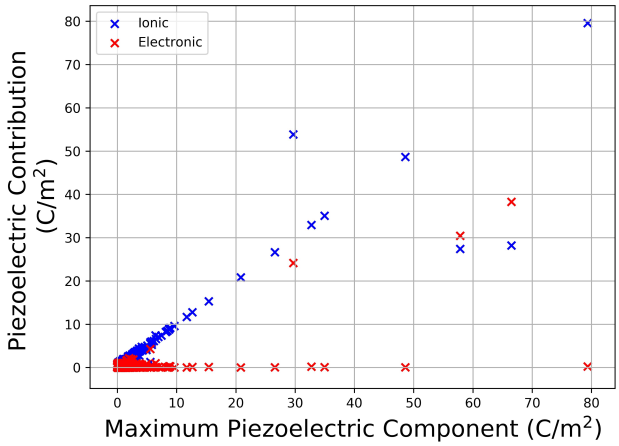

Figure A.1.1: The absolute values of the electronic and ionic contributions to the highest component of the piezoelectric tensor for 1106 materials in the Materials Project as of 2017. The ionic component contributes nearly all of the effect for most materials. For materials in which the electronic contribution is significant, we still see a large contribution from the ionic portion.

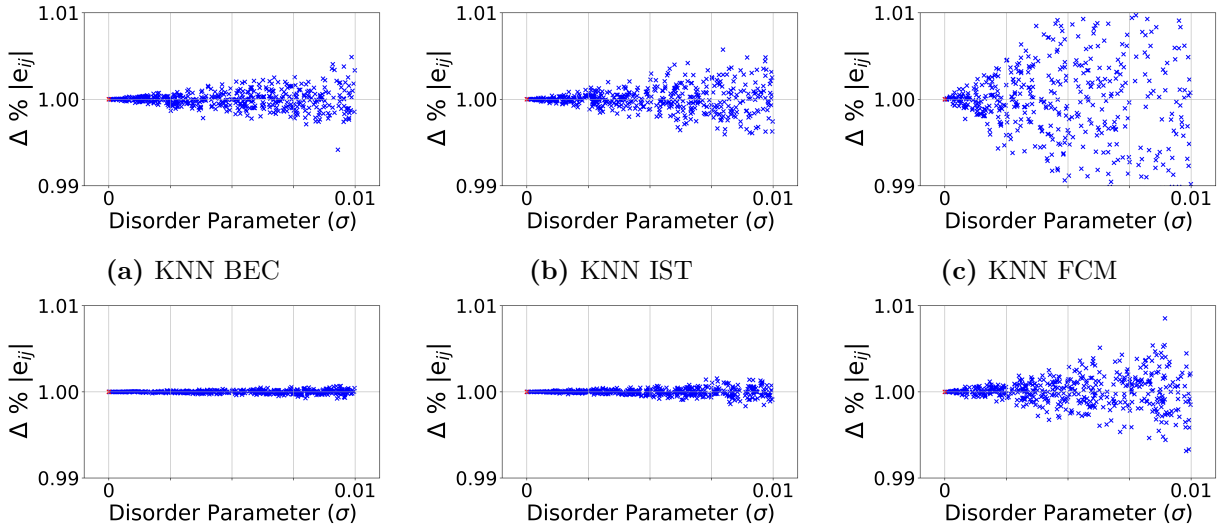

(a) KNN BEC **(b)** KNN IST **(c)** KNN FCM

(d) BNT BEC **(e)** BNT IST **(f)** BNT FCM

Figure A.1.2: The effect of σ on the maximum component of the piezoelectric tensor when applied to the born effective charges, internal strain tensor, and force constant matrix for KNN and BNT. The highlighted cone around the data spread is used as a guide for the eye.

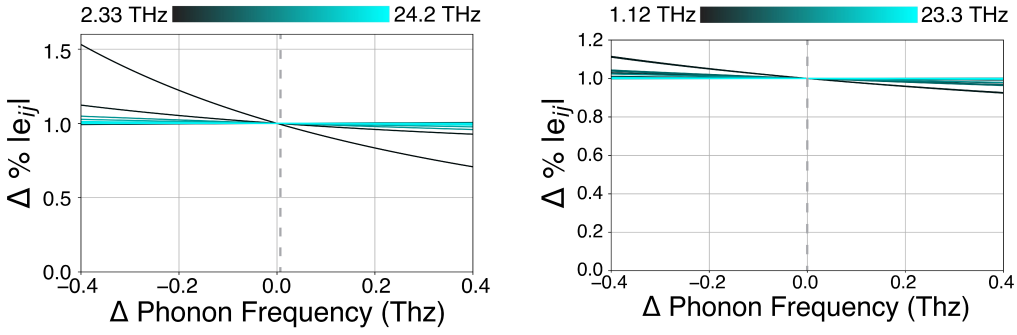

(a) KNN phonon modes **(b)** BNT phonon modes

Figure A.1.3: The phonon frequencies of $K_{0.5}Na_{0.5}NbO_3$ and $Bi_{0.5}Na_{0.5}TiO_3$ are varied independently to determine the effect of each individual mode on the piezoelectric tensor.

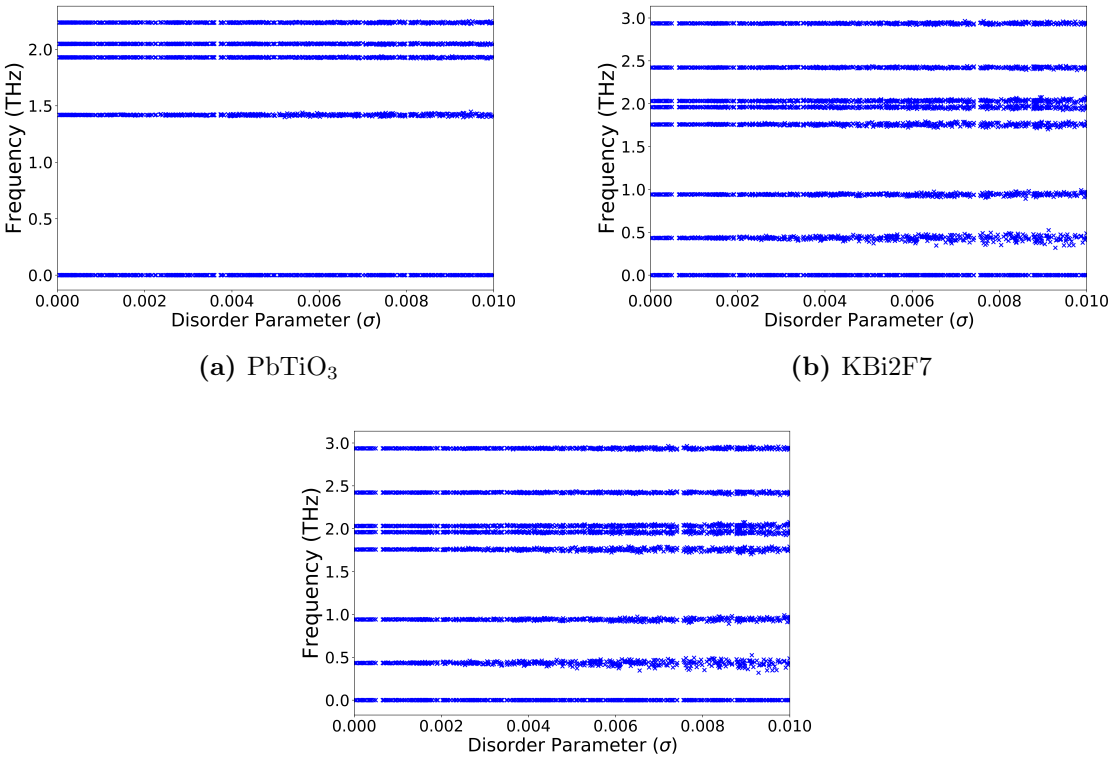

(a) $PbTiO_3$

(b) KBi2F7

(c) Pr3NF6

Figure A.1.4: The effect of the disorder parameter on the low freqency phonon spectra of (a) $PbTiO_3$, (b) KBi_2F_7, and (c) Pr_3NF_6. In general, the disorder parameter causes a broadening of phonon frequencies, although the origin of the magnitude of broadening on each phonon mode requires further investigation.

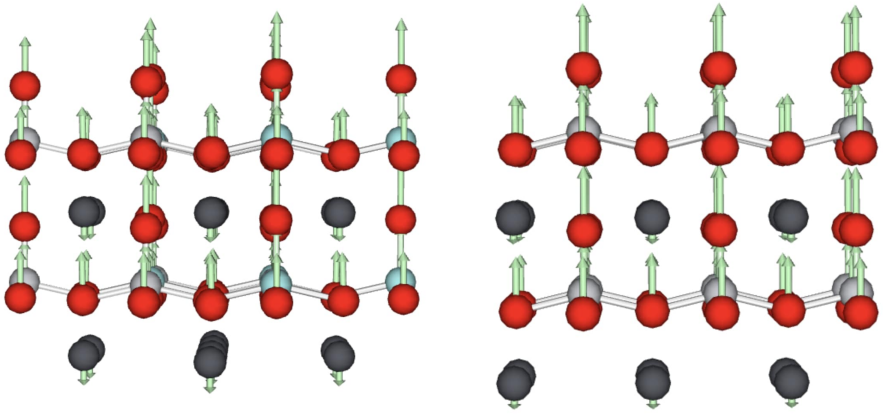

(a) PZT optical phonon mode

(b) $PbTiO_3$ optical phonon mode

Figure A.1.5: The optical mode which most dramatically effects the piezoelectric response in PZT is shown along with its analogue in $PbTiO_3$ visualized through the Phonon Website (http://henriquemiranda.github.io/phononwebsite/). The force constants were calculated through DFPT as defined in procedures. The frequency of the phonon mode is 4.51 THz in PZT and 4.91 THz in $PbTiO_3$ suggesting that the softening of this mode facilitates the increase in piezoelectric response. Pb atoms are shown in black, O in red, Ti in grey, and Zr in teal.

Formula	Cation / Anion Ordering	Lowest Optical Phonon (Thz)	e_{ij} Max (C/m^2)	Single/Multiple Contributing Modes
KBi_2F_7	1	0.433	12.76	Single
–	2	0.850	1.42	–
–	3	0.767	1.49	–
Pr_3NF_6	1	0.171	48.66	Single
–	2	2.49	0.37	–
–	3	2.49	0.37	–
–	4	1.91	2.06	–
–	5	2.49	0.39	–
–	6	1.91	2.06	–
–	7	2.24	0.38	–
$TlNO_2$	1	0.342	9.056	Single
–	2	1.24	0.647	–
–	5	2.00	0.764	–
$NaBiS_2$	1	1.04	9.173	Multiple
–	2	1.54	5.598	–
$PbTi_{0.5}Zr_{0.5}O_3$	1	0.76	6.866	Multiple
–	2	1.06	6.670	–
–	3	0.76	6.791	–

Table A.1.1: Effect of altering the identified optical phonon frequencies in KBi_2F_7 and Pr_3NF_6 as a result of changing the cation ordering. Shown are the lowest optical frequency and the magnitude of the largest piezoelectric tensor component for different cation orderings.

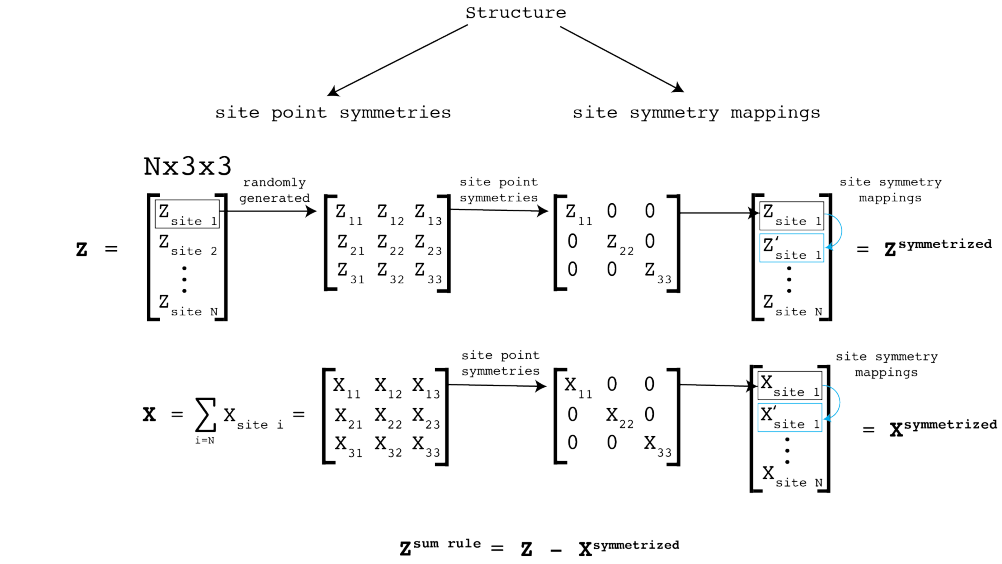

(a) Stochastic Born effective charge tensor generation

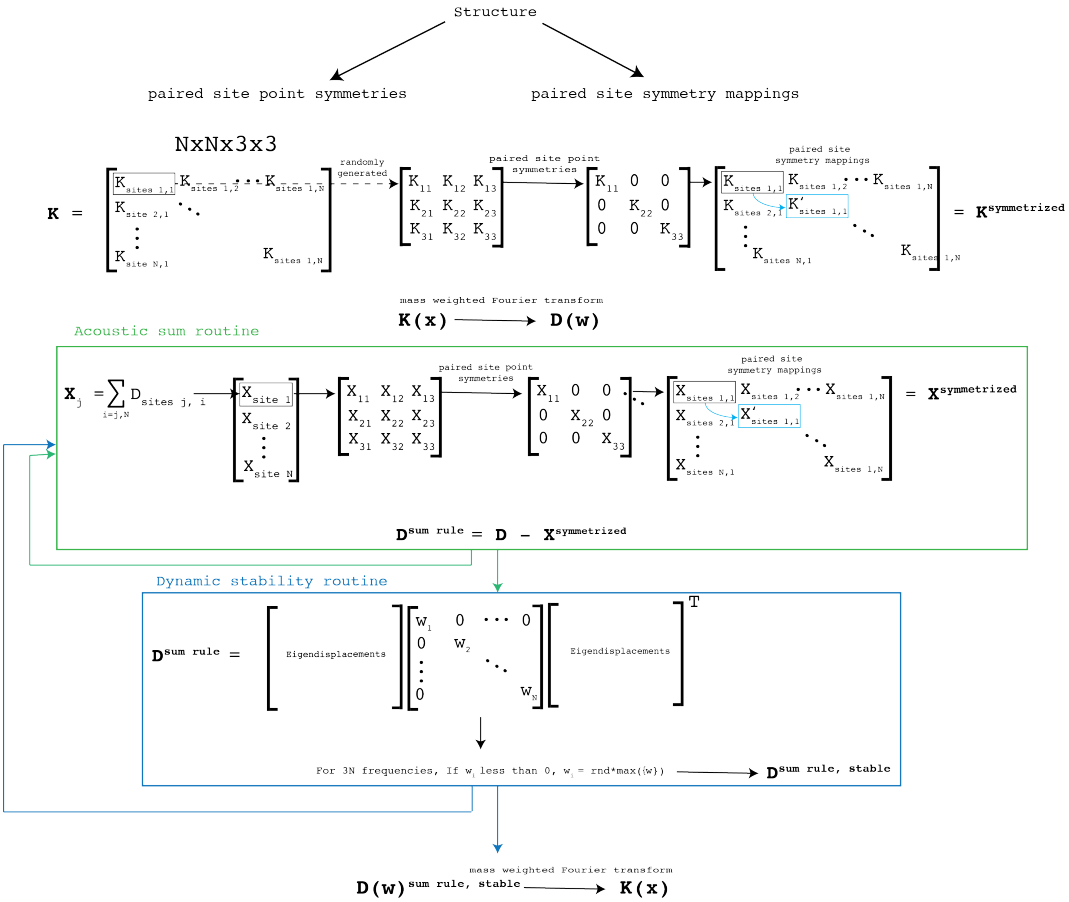

(b) Stochastic force constant matrix generation

Figure A.1.6: The generation of stoachastically generated tensors is diagrammed for the (a) Born effective charge and (b) force constant matrix. The internal strain tensor is generated in the exact same manner as the Born effective charge without the sum rule enforced.

A.2 Additional Details for Chapter 3

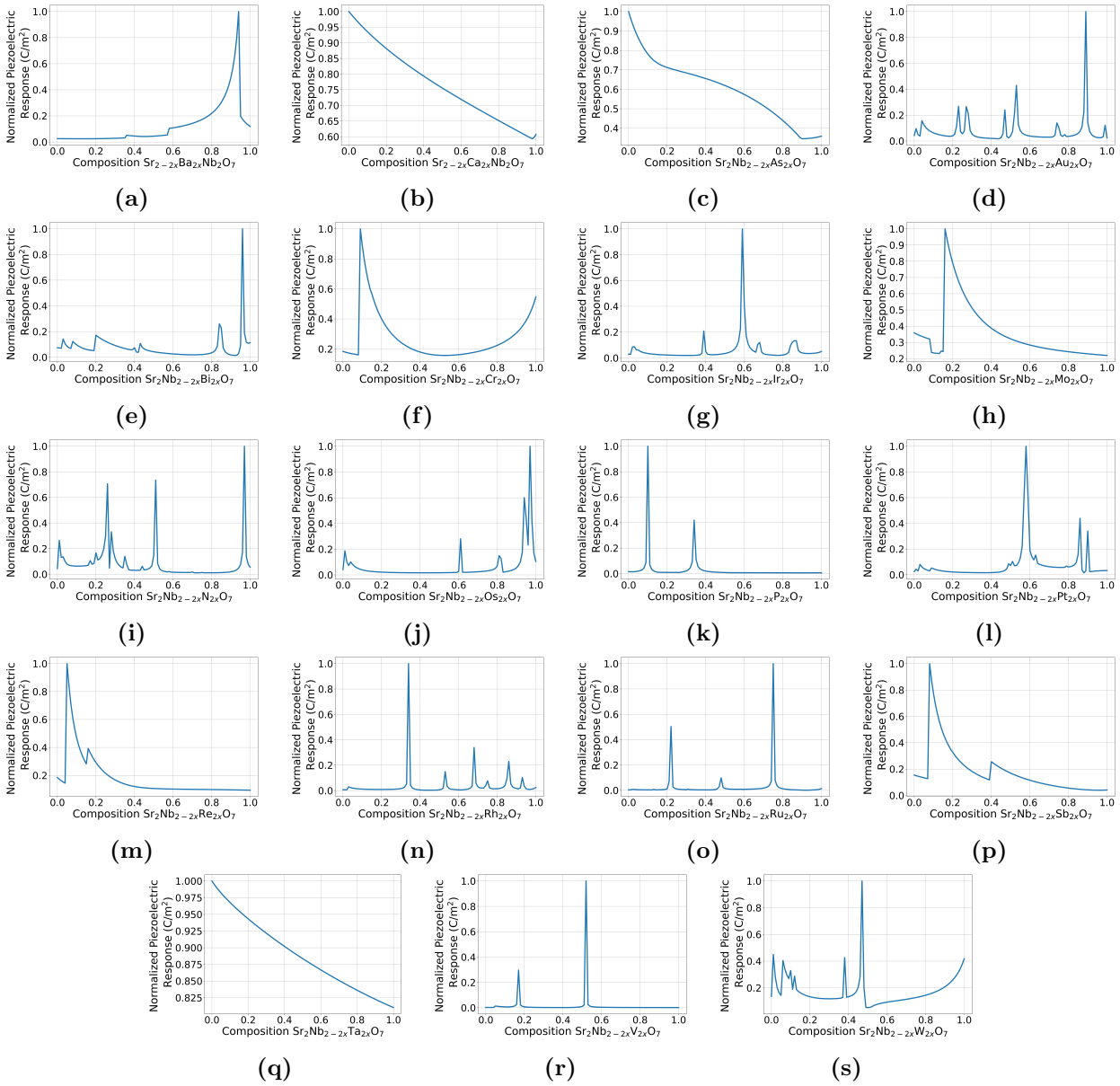

Figure A.2.1: The approximated piezoelectric response for $Sr_{2-2x}A_{2x}Nb_2O_7$ and $Sr_2Nb_{2-2x}B_{2x}O_7$ alloys, where A = {Ca, Ba} and B = {As, Au, Bi, Cr, Ir, Mo, N, Os, P, Pt, Re, Rh, Ru, Sb, Ta, V, W} using the interpolated force constant matrices, Born effective charges, and internal strain tensor properties for intermediate compositions.

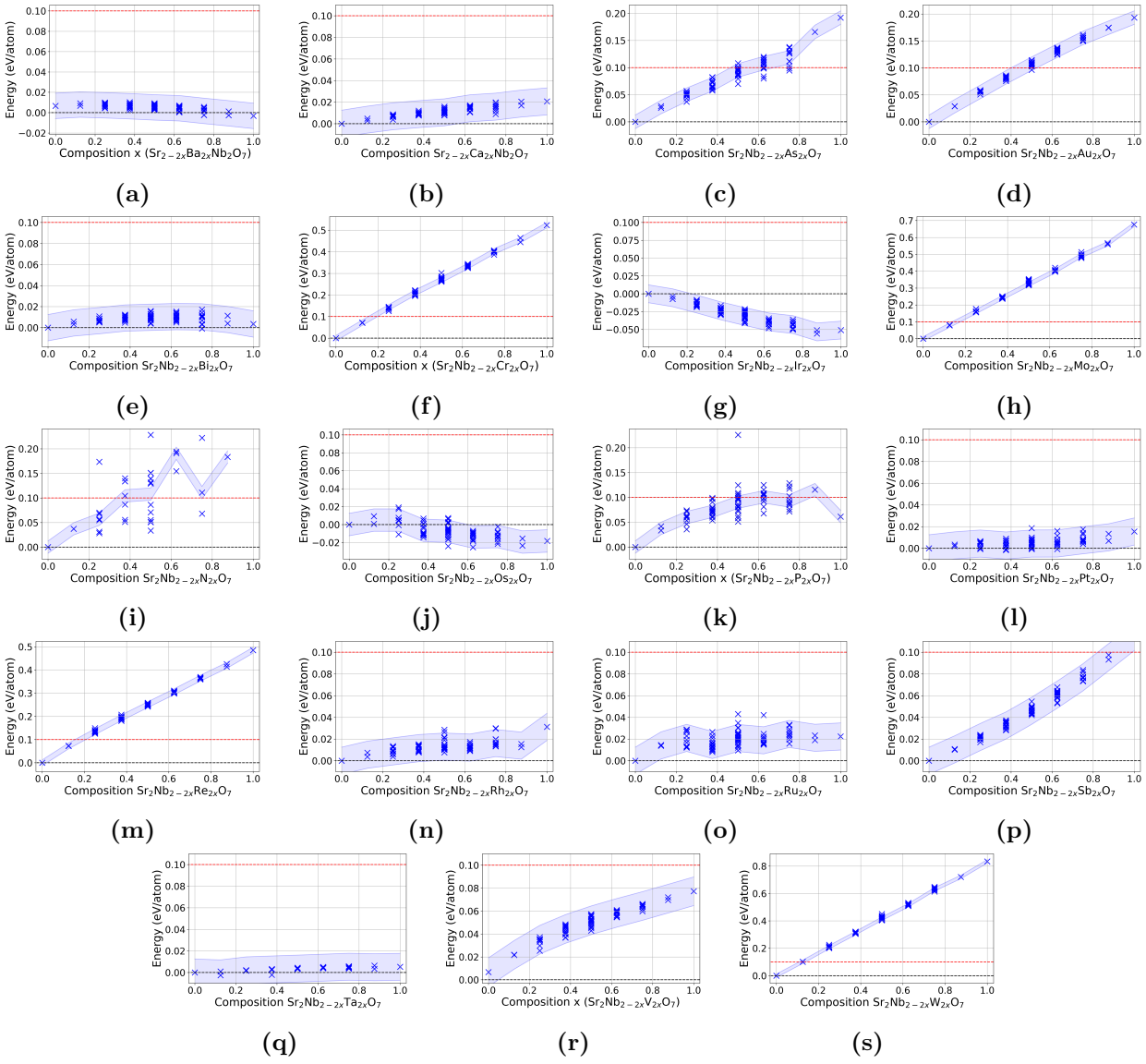

Figure A.2.2: The energy above hull for various orderings of $Sr_{2-2x}A_{2x}Nb_2O_7$ and $Sr_2Nb_{2-2x}B_{2x}O_7$ alloys, where A = {Ca, Ba} and B = {As, Au, Bi, Cr, Ir, Mo, N, Os, P, Pt, Re, Rh, Ru, Sb, Ta, V, W}. These energies are used to determine the solid solution stability and metastability of potential alloy systems

A.3 Additional Details for Chapter 4

Comparison of XRD Figures of Merit: Peak Values vs. Full Pattern

The objective function for matching XRD patterns in the manuscript is given by:

$$R_{peaks} = \sum_{peaks} (I_t - I_c)^2 / \sum_{peaks} I_t \tag{A.3.1}$$

where I_c and I_t are the intensities of calculated candidate peaks and target peaks, respectively, and I_c peak values within 0.15° 2θ of each I_t peak are included in the sum. Alternate objective functions may be used within the AXS framework, and here we also demonstrate AXS coupled with an objective function that accounts for the full pattern, and is not limited to the indexed peak values:

$$R_{full} = \sum_{2\theta} |I_t - I_c| / \sum_{2\theta} I_t \tag{A.3.2}$$

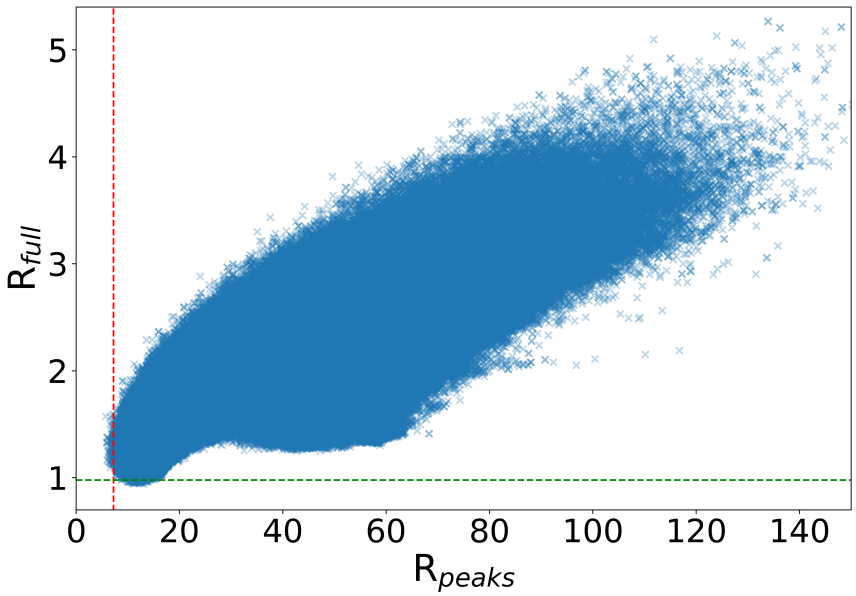

Figure A.3.1

Figure A.3.2: Comparison between the R_{full} and R_{peaks} metric for structures generated through AXS at density H = 2, This collision tolerance parameter which defines atomic overlap, `d_tol` = 1.5. The red and green dashed line represent the cut-off for the 100 lowest structures with best match to the target XRD pattern as defined by the R_{peaks} and R_{full} functions respectively.

where the sum includes all two theta values in the pattern. These objective functions are also used by the FPASS structure solution algorithm.[88]

In this example, to compute R_{full}, we simulate the point intensities for the experimental powder diffraction pattern of $LiFeO_2$ starting with the experimental stick pattern and using default settings on the ICDD PDF; we simulate full XRD patterns for candidate structures by applying a Gaussian to the stick patterns generated from the AXS structures through pymatgen.[89] The comparison of R_{peaks} and R_{full} for $LiFeO_2$ candidate structures is shown in Figure A.3.1 Although there is not overlap between these 100 lowest structures generated by each metric, there is a strong positive correlation between R values.

Focusing on the R values for the best 100 candidate structures, which are those sent for DFT relaxation, in Figure A.3.3 we plot the normalized RMS distance between candidate structures and the final solved structure from AXS reported in our manuscript. For candidates filtered by the two different choices of R value, the normalized RMS distance from the solved structure lies within a similar range.

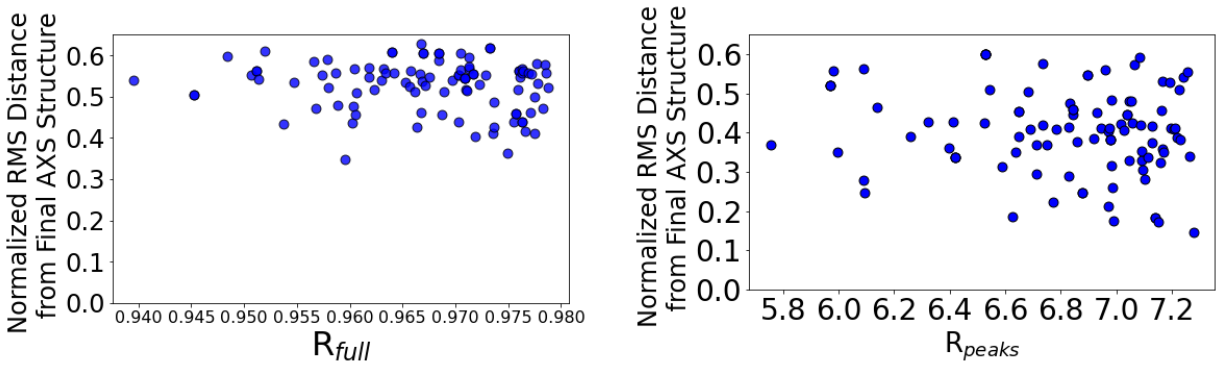

(a) **(b)**

Figure A.3.3: The normalized RMS distance for each of the 100 lowest structures generated from AXS using the both R_{full} and R_{peaks}.

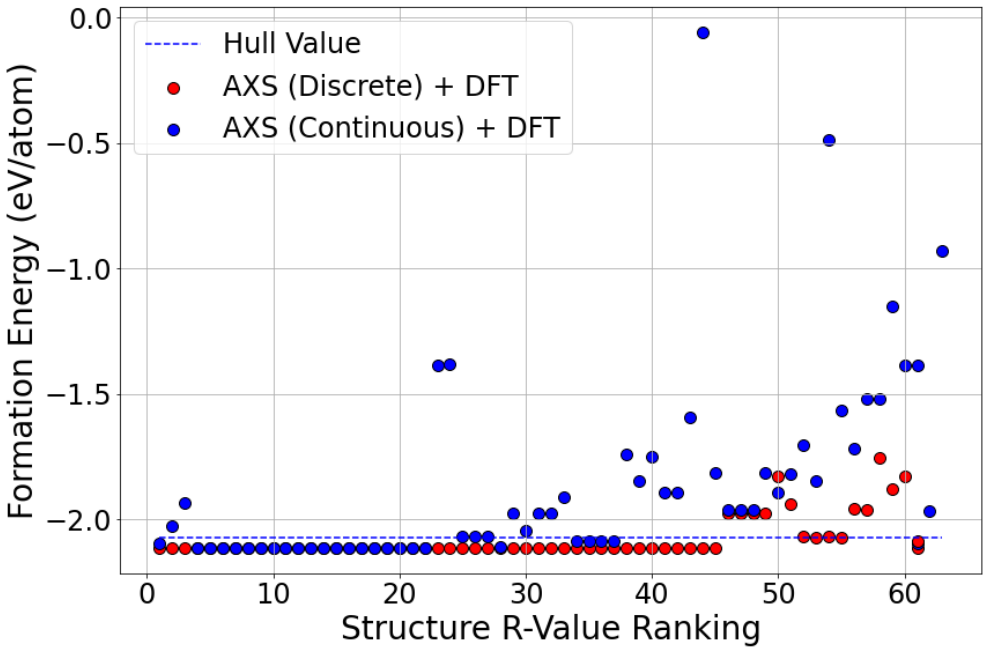

Figure A.3.4: We plot the formation energies of DFT relaxed structure which AXS would generate with R_{full} as compared to those generated by the R_{peaks} objective function.

Finally, we compare the solved structures from AXS using R_{full} vs. R_{peaks}, and find that the lowest energy structures are the same. We also note that the R_{full} metric takes approximately 6 times longer to calculate.